arXiv:astro-ph/0501261v1 13 Jan 2005

First Results from the CHARA Array. I. An Interferometric and Spectroscopic Study of the Fast Rotator α Leonis (Regulus)

H. A. McAlister, T. A. ten Brummelaar, D. R. Gies[1], W. Huang[1], W. G. Bagnuolo, Jr., M. A. Shure, J. Sturmann, L. Sturmann, N. H. Turner, S. F. Taylor, D. H. Berger, E. K. Baines, E. Grundstrom[1], C. Ogden

Center for High Angular Resolution Astronomy, Georgia State University, P.O. Box 3969, Atlanta, GA 30302-3969

hal@chara.gsu.edu, theo@chara-array.org, gies@chara.gsu.edu, huang@chara.gsu.edu, bagnuolo@chara.gsu.edu, mashure@yahoo.com, judit@chara-array.org, sturmann@chara-array.org, nils@chara-array.org, taylor@chara.gsu.edu, berger@chara-array.org, baines@chara.gsu.edu, erika@chara.gsu.edu, ogden@chara.gsu.edu

S. T. Ridgway

Kitt Peak National Observatory, National Optical Astronomy Observatory, P.O. Box 26732, Tucson, AZ 85726-6732

sridgway@noao.edu

and

G. van Belle

Michelson Science Center, California Institute of Technology, 770 S. Wilson Ave, MS 100-22, Pasadena, CA 91125

gerard@ipac.caltech.edu

ABSTRACT

We report on K-band interferometric observations of the bright, rapidly rotating star Regulus (type B7 V) made with the CHARA Array on Mount Wilson,

[1]Visiting Astronomer, Kitt Peak National Observatory, National Optical Astronomy Observatory, operated by the Association of Universities for Research in Astronomy, Inc., under contract with the National Science Foundation.

California. Through a combination of interferometric and spectroscopic measurements, we have determined for Regulus the equatorial and polar diameters and temperatures, the rotational velocity and period, the inclination and position angle of the spin axis, and the gravity darkening coefficient. These first results from the CHARA Array provide the first interferometric measurement of gravity darkening in a rapidly rotating star and represent the first detection of gravity darkening in a star that is not a member of an eclipsing binary system.

Subject headings: stars: fundamental parameters — stars: individual (Alpha Leo, Regulus) — stars: rotation — infrared: stars — techniques: interferometric

1. Introduction

1.1. The CHARA Array

Georgia State University's Center for High Angular Resolution Astronomy (CHARA) operates an optical/IR interferometric array on the grounds of Mount Wilson Observatory in the San Gabriel Mountains of southern California. The six light-collecting telescopes of the CHARA Array, each of 1-m aperture, are distributed in a Y-shaped configuration providing 15 baselines ranging from 34.1 to 330.7 m. Three of these baselines formed by the outer telescopes of the Y are in excess of 300 m. Ground breaking for the facility occurred in 1996 July, and the sixth and final telescope became fully integrated into the Array in 2003 December, thus signaling completion of construction and readiness for ongoing science observations. Numerous technical reports and updates have been published throughout the design and construction phases of this project, the most recent of which is by McAlister et al. (2004), with many internal project reports available at CHARA's website[2]. A companion paper (ten Brummelaar et al. 2004) describes the full complement of technical and performance details of the instrument.

With its long baselines, currently the longest operational K-band baselines in the world, and its moderate apertures, the CHARA Array is well positioned for observations of main sequence stars not previously accessible to such high-resolution scrutiny. CHARA inaugurated its first diverse observing season in the spring of 2004 with a fully scheduled semester of science observations targeting stellar diameters, young stellar objects, and rapidly rotating stars. That semester was immediately preceded by an observing campaign directed entirely

[2]http://www.chara.gsu.edu/CHARA/techreport.html

at Regulus, a very rapidly rotating star expected to exhibit marked rotational oblateness and a resulting surface flux variation associated with gravity darkening. This paper is a report of the outcome of those observations of Regulus and represents the first scientific results from the CHARA Array.

1.2. Regulus

The star Regulus (α Leo, HR 3982, HD 87901) is of spectral type B7 V (Johnson & Morgan 1953) or B8 IVn (Gray et al. 2003), and is a well-known rapid rotator. The difficulty of determining the projected rotational velocity $V \sin i$ is exemplified by the wide range of values published for this star, with velocities in the literature ranging from 249 ± 9 km s^{-1} (Stoeckley, Carroll, & Miller 1984) to 350 ± 25 km s^{-1} (Slettebak 1963). The first attempts to model realistically a line profile derived from a rotating star were by Elvey (1930) who employed the method proposed by Shajn & Struve (1929) based upon dividing a photosphere into strips whose Doppler shifted contributions are weighted by the relative areas of these strips. Slettebak (1949) very significantly extended this analysis for rapidly rotating O and B stars to include the effects of limb darkening, gravity darkening based on Roche models incorporating the von Zeipel Effect (von Zeipel 1924), and differential rotation. Slettebak (1966) subsequently showed that the envelope of the most rapidly rotating stars of a given spectral type most closely approached the threshold of breakup velocities for stars of early- to mid-B type. Regulus clearly falls in the domain of stars rotating close to breakup speed and can thus be expected to show significant rotationally induced oblateness and gravity darkening.

The Washington Double Star Catalog[3] lists three companions to Regulus, none of which has exhibited significant orbital motion since its first detection. The B component, ~ 175 arcsec from Regulus, is HD 87884, a K2 V star whose proper motion, radial velocity and spectroscopic parallax are consistent with its being a physical rather than optical companion. On the other hand a comparison of ages of components A and B has found the discordant values of 150 and 50 Myr, respectively (Gerbaldi, Faraggiana, & Balin 2001). Component B is accompanied by a faint companion ($V = +13.1$) comprising the subsystem BC that closed from 4.0 arcsec to 2.5 arcsec during the period 1867 to 1943 and has apparently not been measured in the last 60 years. At the distance of Regulus, the apparent magnitude of component C implies a star of approximate spectral type M4 V. Only a single measurement exists for a D component, more than 200 arcsec from Regulus, whose existence as a physical

[3]http://ad.usno.navy.mil/wds/wds.html; maintained at the U. S. Naval Observatory

member of the α Leo system might therefore be suspect.

The Bright Star Catalog (Hoffleit 1982) notes that Regulus is a spectroscopic binary. We have found no reference to this in the literature except a flag in the bibliographic catalog of Abt & Biggs (1972) indicating the "progressive change" of radial velocity as reported by Maunder (1892). After conversion to modern units (Maunder used German geographical miles per second), the measured velocities declined from +40 km s^{-1} to −9 km s^{-1} between 1875 and 1890. In light of the difficulty of accurately measuring velocities from hydrogen lines compounded by the very high rotational speed and the state of the art of the technique more than a century ago, the conclusion that those data indicate orbital motion seems unlikely. Furthermore, the General Catalogue of Stellar Radial Velocities (Wilson 1963) does not flag the star as a spectroscopic binary. On the other hand, Regulus may represent a case of neglect by radial velocity observers due to its brightness and extreme rotational broadening. If the velocities were to hint at a closer companion than the AB system, the corresponding orbital period would be on the order of a year with a separation in the range 50 to 70 mas, the regime of detectability by speckle interferometry. However, no closer companions have been reported from lunar occultation observations or from the CHARA speckle interferometry survey of bright stars (McAlister et al. 1993). In this angular separation regime, the fringe packets from Regulus and a very much fainter close companion would be non-overlapping in the fringe scan, and the companion's presence would have no effect on our analysis of stellar shape and surface brightness. One of the goals of this study has been to determine the orientation of the spin axis of Regulus. Owing to the lack of sufficient motion within the Regulus multiple star system and the apparent lack of any unknown closer companions, it will not be possible to compare rotational and orbital angular momentum vectors.

Regulus possesses an intrinsic brightness and relative nearness to the Sun to make it an ideal candidate for diameter determination from long-baseline interferometry. Therefore, the star was among the classic sample of bright stars whose diameters were measured by Hanbury Brown and his colleagues at the Narrabri Intensity Interferometer nearly four decades ago (Hanbury Brown 1968; Hanbury Brown et al. 1967; Hanbury Brown, Davis, & Allen 1974). In the first of these papers, the implications of a very high rotational velocity for the derived diameter were clearly recognized and discussed semi-quantitatively, but the resulting diameter of 1.32±0.06 mas, measured at λ = 438.5 nm for a uniform disk (UD), was judged to incorporate insufficient baseline sampling to be interpreted as other than circularly symmetric. A value of 1.37±0.06 mas was determined for a limb-darkened disk (LD). Because gravity darkening brightens the poles and thus counteracts the star's oblateness, it was thought that the maximum change in apparent angular diameter within the primary lobe was only 6%, which was judged to be marginal to detect in those observations. Furthermore, measurements beyond the first lobe were impossible because of the limited sensitivity of the

Narrabri instrument (in which the response varies as the square of the visibility).

The other direct measurements of the angular diameter of Regulus come from lunar occultations. Although an early measurement (Berg 1970) yielded a diameter of 1.7±0.5 mas, the only two reliable measurements of Regulus have been made by Radick (1981) and Ridgway et al. (1982). Radick (1981) obtained a diameter of 1.32±0.12 mas (UD) at λ = 576.8 nm and 1.37±0.11 (UD) at λ = 435.6 nm. These translate to 1.36 and 1.43 mas (LD), respectively. The angle of local moon normal to the star was small, thus this observation sampled the minor axis of the star. A second set of observations obtained several months later at KPNO by Ridgway et al. (1982) with the 4-m telescope in H-band (1.67 μm) lead to a diameter of 1.44±0.09 mas (UD) or 1.46 (LD). The angle of approach was somewhat steeper in this instance, about 32° (D. Dunham, 2004, private communication). It is tempting to suppose that the somewhat higher value in this case is due to the geometry, but the observations obviously agree within stated errors. The simple average of all three observations (averaging the two from Radick) is 1.42 mas (LD), which agrees well with our diameter measurements discussed below.

A detailed consideration of the response of a long-baseline interferometer to a rotationally distorted star was first undertaken by Johnston & Wareing (1970) who identified Regulus and Altair (α Aql), along with the somewhat fainter star ζ Oph, as nearly ideal targets for an interferometer with sensitivity beyond that of the Narrabri instrument. They argued that the high projected rotational velocities of these stars implied inclinations of their rotational axes with respect to the line of sight of nearly 90°.

Two rapidly rotating stars have now been observed with the new generation of interferometers envisioned by Johnston & Wareing (1970). Van Belle et al. (2001) have used the Palomar Testbed Interferometer (PTI) to measure the oblateness of Altair and to derive a $V \sin i$ independent of spectroscopy on the basis of a rapidly rotating Roche model to which the measured interferometric visibilities were fit. The PTI results led to the determination of the star's polar diameter of 3.04±0.07 mas with an equatorial diameter 14% larger. The Very Large Telescope Interferometer (VLTI) has been used by Domiciano de Souza et al. (2003) to study the oblateness of the Be star Achernar (α Eri). A rotating Roche model with gravity darkening was applied to the collective VLTI visibilities following an initial simplified uniform disk diameter fit to individual visibilities with the conclusion that the Roche approximation does not pertain in the case of Achernar. Achernar was found to have a polar angular diameter of 1.62±0.06 mas with an extraordinary oblateness ratio of 1.56±0.05.

The smaller diameter of Regulus in comparison with Altair and Achernar calls for an interferometer with baselines longer than those possessed by the PTI and VLTI instruments. At the longest baselines of the CHARA Array, access is obtained in the K-band infrared

to visibilities descending to the first null in the regime in which the departures from a uniform disk expected for a rapid rotator become increasingly more pronounced. With this in mind and inspired by the interest generated from the PTI and VLTI results, Regulus was selected as an ideal target for an extensive observing campaign with the CHARA Array. The combination of the resulting CHARA interferometric data with a number of constraints resulting from spectroscopy of Regulus have permitted us to determine the star's polar and equatorial angular diameters and temperatures, inclination angle of the spin axis with respect to the line of sight, position angle of the spin axis in the plane of the sky, equatorial rotational velocity, and gravity darkening index.

2. Interferometric Observations

Regulus was observed on a total of 22 nights between 2004 March 10 and 2004 April 16 using 10 of the 15 baselines available from the CHARA array. A calibrator star, HD 83362 (G8 III, $V = +6.73$, $K = +4.60$), was selected on the basis of its predicted small angular diameter and its lack of known stellar companions. This star is located $7\overset{\circ}{.}4$ from Regulus. No suitable calibrator was found closer in angular separation. A third object, HD 88547 (K0 III, $V = +5.78$, $K = +2.97$), was chosen as a check star on the basis of having a predicted angular diameter comparable to that of Regulus but not expected to show rotational oblateness due to its low $V \sin i = 2.5 \pm 0.8$ km s^{-1} (Henry et al. 2000). These three objects were observed in a sequence so as to provide a series of time-bracketed observations permitting the conversion from raw to calibrated visibility for each observation of Regulus and the check star.

All observations were obtained in the K-band infrared using a K'-band filter whose effective wavelength was determined to be 2.1501 μm for a star of spectral type B7. This value is based upon the atmospheric transmission, the measured filter transmission, the detector DQE, and from data provided by the vendors for the various optical surfaces encountered along the light path of each arm of the interferometer. The stellar photon count rate is also included, and the increase in effective filter wavelength to 2.1505 μm for the late-type giants is considered to be negligible here.

Interference fringes were obtained using a classical two-beam interferometer configuration in which light is detected emerging from both sides of a beam splitter with a PICNIC HgCdTe 256×256 hybrid focal plane array (sensitive to the wavelength range 1.0 to 2.5 μm) developed by Rockwell Scientific Company (Sturmann et al. 2002). After open-loop path length difference compensation is attained with the optical delay lines, the zero path difference position is scanned with a dither mirror in order to produce fringes of a selectable frequency, with 150 Hz fringes being utilized for all the data in this analysis. A single dataset

consists of some 200 fringe scans preceded and followed by shutter sequences to measure the light levels on each input side of the beam splitter. These sequences permit the calculation of a visibility adjustment factor to correct for any imbalance between the two detected signals (Traub 2000). Such a dataset requires approximately five minutes of observing time.

2.1. Visibility Measurement

Methods of extraction of visibilities from these data are discussed in detail in Paper II (ten Brummelaar et al. 2004) and generally follow the procedures described by Benson, Dyck, & Howell (1995). For the data obtained here, the correlation ν, measured from fringe amplitude, is treated as the proxy for visibility V. Algorithms were developed for seeking the interference fringe in each scan by locating the maximum excursion from mean intensity within the scan. Identification of false features in each scan can be a problem at low SNRs, and several methods were applied to guard against this. These include the tracking of the location of the fringe center, which should wander through successive scans in a continuous fashion, and calculating a SNR for each detected fringe based upon the amplitude of the peak in the power spectrum for that fringe. When a detected fringe is considered to be real, the amplitude of that fringe is determined by mathematical fitting of the fringe, and the amplitude of the fit is adopted as the correlation ν. This means that the entire fringe packet, not just the maximum in the packet, contributes to the measurement of ν. The sequence of fringe scans in a given dataset is subdivided by time into 15 subsets from which 15 mean values of ν are calculated, and the final value of ν and its standard error associated with a given dataset are taken as the mean and standard deviation arising from the 15 subsets.

The conversion of a correlation measured from fringe amplitude to a visibility is achieved by dividing the correlation of the calibrator star obtained by time interpolation between calibrator observations immediately before and after the target star. This is the standard practice in optical interferometry to compensate for the time varying transfer function arising primarily from atmospheric fluctuations. It assumes a known value for the angular diameter of the calibrator whose predicted visibility can then be multiplied by the ratio of the target to calibrator correlations to obtain the visibility of the target star.

Estimating the visibility of the calibrator star (in this case HD 83362) is a critical factor in any interferometric diameter analysis. We have obtained a reliable estimate of the diameter of the calibrator by utilizing the relationship existing among the parameters angular diameter, effective temperature, and surface flux. Thus, we have calculated an estimated angular diameter for the calibrator star HD 83362 by fitting to a spectral energy

distribution selected according to spectral type from a template compiled by Pickles (1998) to the available broadband photometry, particularly in the near-infrared (Gezari et al. 1993; Cutri et al. 2003). The resulting angular diameter for HD 83362 is 0.516±0.032 mas (UD), and we adopted this value for the calibration of visibilities for Regulus and the check star HD 88547. The error in the estimated diameter for the calibrator star is ±6.2%, and this propagates into the measurements for the check star to produce ±0.9% and ±2.5% errors in calibrated visibility for baselines of 200 m and 300 m, respectively. For the larger diameter of Regulus, these errors are reduced to ±0.5% and ±2.2%. The errors in derived diameters resulting from the uncertainty in the diameter of the calibrator are ±0.8% for the check star and ±0.5% for Regulus. The overall errors in these determinations are significantly larger and dominated by the random error in visibility measurements. The uncertainty in the adopted diameter for the calibrator has a second order, and therefore negligible effect, on interferometric determination of relative shape and relative surface brightness variation.

This approach has led to 69 measurements of calibrated visibilities for Regulus and 40 such visibilities for HD 88547. Those values are summarized in Tables 1 and 2 and are available on the CHARA website in the standard optical interferometry FITS format (Pauls et al. 2004). The distributions in the projected baseline plane are shown in Figure 1. These data are shown plotted in Figure 2 along with the best fits of uniform disk diameters using the standard equation for fitting $V(B)$ to obtain Θ_{UD} (cf. equation 3.41 of Traub 2000). These fits yield $\Theta_{UD,HD88547} =$ 1.29±0.07 mas and $\Theta_{UD,Regulus} = 1.47\pm0.12$ mas. It is apparent from the standard deviations of these values and simple inspection of Figure 2 that, while the diameter fit to the check star is reasonable and in good agreement with the diameter predicted from the available photometry, the fit to Regulus is much poorer with large systematic residuals. This immediately suggests that the interferometry of Regulus cannot be explained in terms of a simple uniform disk model.

2.2. Modelling Visibilities Geometrically

The interferometric analyses of the rapid rotators Altair (van Belle et al. 2001) and Achernar (Domiciano de Souza et al. 2003) discussed the shapes of these stars on the basis of uniform disk diameter values associated with each V^2 prior to subjecting their data to more sophisticated models. Using this same approach as a starting point, we have selected observations made at the longest baselines that are clustered in several position angle regions as indicated in Figure 1. There are 6, 5, and 6 measurements of V respectively in these clusters, and they yield UD diameters for Regulus of 1.413±0.024 mas, 1.514±0.028 mas, and 1.328±0.028 mas for the three mean position angles 129.°1, 181.°3, and 251.°6, respectively.

A similar treatment of observations of the check star HD 88547 results in UD diameters of 1.233±0.012 mas, 1.260±0.057 mas, and 1.246±0.015 mas at position angles 128.°8, 206.°8, and 253.°4. These diameters are shown plotted in Figure 3 which clearly suggests that the check star is round while Regulus exhibits an elongated shape whose major axis is oriented along a position angle roughly in the range of 150° to 180°.

We next fitted the visibility data with a series of elliptical models of constant surface brightness, which we label as UE fits to distinguish from UD models. These models have the advantage that their Fourier transform is just an Airy function, elongated according to the axial ratio (Born & Wolf 1999). These fits are a natural extension to the UD models done traditionally for (circular) stellar diameters. Indeed, the fact that UE models are, like UD fits, Airy functions is why one may reasonably take the approach of the previous paragraph for a star whose shape is approximated by an ellipsoid. This three-parameter approach yields a best-fit UE model with $R_{\rm minor}/R_{\rm major} = 0.845 \pm 0.029$, a mean diameter of 1.42 ± 0.04 mas (or $R_{\rm minor} = 0.651$, $R_{\rm major} = 0.771$ mas), a position angle of the short axis of the ellipse of $84.^{\circ}90 \pm 2.^{\circ}4$ (measured eastward from north), and a reduced chi-square value of 3.41. These results indicate that the star is clearly non-spherical in shape, and in the following section we develop a physical model for the star so that we can make a realistic comparison between the predicted rotationally distorted shape and the observed visibilities.

3. Spectroscopic Constraints on the Physical Parameters of Regulus

Rapid rotation in stars like Regulus has two immediate consequences for a physical description of the star. First, the star will become oblate, and thus we need a geometrical relationship for the star's radius as a function of angle from the pole. Secondly, the surface temperature distribution will also become a function of co-latitude, usually assumed to be cooler at the equator than at the poles. Reliable estimates of the predicted stellar flux, spectral features, and angular appearance in the sky will then be functions of nine parameters: mass M, polar radius R_p, polar effective temperature T_p, equatorial velocity V_e, inclination angle of the pole to the line of sight i, position angle α of the polar axis from the north celestial pole through the east at the epoch of observation, gravity darkening exponent β that defines the amount of equatorial cooling (Collins et al. 1991), distance to the star d, and interstellar extinction. In principle one can make a grid search through these parameters to find the best-fit of the interferometric visibilities for different baselines projected onto the sky (van Belle et al. 2001), but in the case of Regulus there are a number of spectral observations available that can help to reduce significantly the probable range in these parameters. Here, we discuss how the spectral flux distribution and the appearance of several key line profiles

can be analyzed to form these additional constraints that we will apply to the analysis of the interferometric visibility data.

We developed a physical model for the star by creating a photospheric surface grid of 40000 area elements. We assume that the shape of the star is given by the Roche model (i.e., point source mass plus rotation) for given equipotential surfaces based on the ratio of equatorial to critical rotational velocity V_e/V_c (Collins et al. 1991). The effective temperature is set at each co-latitude according to the von Zeipel law (von Zeipel 1924), in which the temperature varies with the local gravity as $T(\theta) = T_p(g(\theta)/g_p)^\beta$ and β is normally set at 0.25 for stars with radiative envelopes (Claret 2003). The model integrates the specific intensity from all the visible surface elements according to their projected area, temperature, gravity, cosine of the angle of the surface normal to the line of sight (μ), and radial velocity. The intensity spectra were calculated over the full range of interest in steps of 2000° in temperature, 0.2 dex in $\log g$, and 0.05 in μ. The spectra were computed using the code *Synspec* (Lanz & Hubeny 2003) and are based on solar abundance atmospheres models by R. L. Kurucz[4] (for a chosen microturbulent velocity of 1 km s^{-1}). The model incorporates both limb darkening and gravity darkening and provides reliable line profiles even in cases close to critical rotation (Townsend, Owocki, & Howarth 2004). Each model spectrum is convolved with an appropriate instrumental broadening function before comparison with observed spectra. The code is also used to produce monochromatic images of the star in the plane of the sky.

We begin by considering the full spectral flux distribution to develop constraints on the stellar radius and temperature. We plot in Figure 4 observations of the flux of Regulus binned into wavelength increments of the same size as adopted in the Kurucz model flux spectrum shown. The measurements for the extreme ultraviolet are from Morales et al. (2001), and the far- and near-ultraviolet spectra are from the archive of the *International Ultraviolet Explorer (IUE) Satellite* (spectra SWP33624 and LWP10929, respectively). The optical spectrophotometry is an average of the observations from Alekseeva et al. (1996) and Le Borgne et al. (2003). The near-infrared fluxes are from the IR magnitudes given by Bouchet et al. (1991) that we transformed to fluxes using the calibration of Cohen et al. (1992). We initially fit this distribution using simple flux models for a non-rotating star, and the fit illustrated in Figure 4 uses the parameters $T_{\rm eff} = 12250$ K, $\log g = 3.5$, $E(B-V) = 0.005$, and a limb-darkened angular diameter of 1.36 ± 0.06 mas. These parameters agree well with those from Code et al. (1976) based upon a full flux integration and the angular diameter from intensity interferometry.

[4]http://kurucz.harvard.edu/

We used the fit of the spectral energy distribution in K-band as the basis of an observational constraint on the integrated flux for our rotating star model. The comparison was made by calculating the K-band flux for a given model and then adjusting the flux according to the distance from the *Hipparcos* parallax measurement of Regulus, $\pi = 42.09 \pm 0.79$ mas or $d = 23.8 \pm 0.4$ pc (Perryman et al. 1997), and the negligible extinction derived from $E(B-V)$ (Fitzpatrick 1999). We require that modeled and observed fluxes agree to better than 1% (the error associated with the fit of the absolute observed flux in the K-band). This constraint primarily affects the selection of the polar temperature (which sets the flux) and polar radius (which together with the adopted distance sets the angular area of the source).

The next constraint is provided by the shape of the hydrogen Hγ λ4340 line profile as shown in Figure 5. This observed spectrum is from the spectral library of Valdes et al. (2004), and it has resolving power of $\lambda/\triangle\lambda = 4900$. This Balmer line grows in equivalent width with declining temperature through the B-star range, and it is wider in dwarfs than in supergiants because of pressure broadening (linear Stark effect). Thus, fits of the profile are set by the adopted model temperature and surface gravity distribution over the visible hemisphere of the star.

Our final constraint is established by the rotational line broadening observed in the Mg II λ4481 line as shown in Figure 6. This spectrum is the sum of 30 spectra obtained in 1989 April with the Kitt Peak National Observatory 0.9-m Coudé Feed Telescope, and it has a resolving power of $\lambda/\triangle\lambda = 12400$. This spectral region also includes the weaker metallic lines of Ti II λ4468, Fe II λ4473, and Fe I λ4476, which become prominent in cooler A-type spectra. All these lines have intrinsically narrow intensity profiles, and the broadening we observe is due primarily to Doppler shifts caused by stellar rotation. A fit of the Mg II λ4481 profile leads directly to the projected equatorial rotational velocity, $V \sin i$, which for a given inclination then defines the actual rotational speed and stellar deformation. Note that we exclude the nearby He I λ4471 line from this analysis, since it is possible that Regulus belongs to the class of He-weak stars that account for about one quarter of the B-stars with temperatures similar to that of Regulus (Norris 1971).

We assume throughout our analysis that the optical and K-band flux originates solely in the stellar photosphere. This assumption needs verification because many rapidly rotating B-type stars develop large equatorially confined disks (spectroscopically identified as Be stars; Porter & Rivinius 2003) and such disks can contribute a large fraction of the K-band flux (Stee & Bittar 2001). The appearance of excess IR flux from a disk is always accompanied by the development of an emission feature in the Balmer Hα profile (Stee & Bittar 2001), so we have searched for any evidence of Hα emission in spectra obtained contemporaneously with the interferometric observations. We show in Figure 7 the average Hα profile in the spectrum

of Regulus formed from 11 spectra obtained with the KPNO Coudé Feed Telescope on 2004 October 13 – 16 (less than six months after our most recently collected interferometric data). This spectrum has a resolution of $R = \lambda/\triangle\lambda = 10600$ and a signal-to-noise ratio of 500 per pixel in the continuum. It appears completely free of any excess emission such as that shown in Figure 7 for two Be stars observed at the same time as Regulus (HD 22780 and HD 210129, both of comparable spectral classification, B7 Vne). We also show in Figure 7 the photospheric Hα profile of a slowly rotating B-star, HD 179761, which we obtained from the spectral atlas of Valdes et al. (2004). This star has a temperature $T_{\rm eff} = 13000$ K and a gravity $\log g = 3.5$ (Smith & Dworetsky 1993) that are comparable to the surface mean values for Regulus. However, it has a very small projected rotational velocity, $V \sin i = 15$ km s^{-1} (Abt, Levato, & Grosso 2002), so we artificially broadened the profile by convolution with a rotational broadening function with $V \sin i = 317$ km s^{-1} (see below) and a linear limb darkening coefficient of 0.30 (Wade & Rucinski 1985) in order to match approximately the line broadening in the spectrum of Regulus. The good agreement between the spun-up version of the Hα profile of HD 179761 and that of Regulus indicates that no excess disk emission is present. We have also examined spectra ($R = 14000$; S/N = 200 – 500) made with the CHARA 1.0-m equivalent aperture Multi-Telescope Telescope (MTT) (Barry, Bagnuolo, & Riddle 2002) on six nights (1999 January 19, March 17, 2000 February 29, April 16, 20, 29), and none of these showed any evidence of emission. Furthermore, another KPNO Coudé Feed spectrum from 2000 December and 21 HEROS spectra (Štefl, Hummel, & Rivinius 2000) made between 2001 May and 2002 May (kindly sent to us by Dr. S. Štefl) are free of Hα emission. These contemporary observations of no emission are generally consistent with the record in the literature. For example, Slettebak & Reynolds (1978) used Regulus as a standard emission-free and non-varying star in a survey for Hα variations among Be stars during the period 1975 December to 1977 June. There is only one report of marginal Hα emission in the spectrum of Regulus in 1981 February (Singh 1982), but the observations at hand indicate that there was no disk at the time of the CHARA Array observations, so that the K-band visibilities can be analyzed reliably in terms of a photospheric model alone.

We constructed a series of stellar models that consistently meet all of these observational constraints for a grid of assumed values of stellar inclination i and gravity darkening coefficient β. The method was an iterative approach in which we first established the projected rotational broadening from fits of the Mg II λ4481 line (dependent only on β over the inclination range of interest) and then progressively approximated the polar temperature and radius to find models that met both the K-band flux and Hγ profile constraints. Note that once the temperature and radius are set, the Hγ fit provides us with the gravity ($\log g$) and hence the final parameter, stellar mass. The results of these solutions for the i and β grid are listed in Table 3, which includes the fitted projected rotational velocity (column 3),

the ratio of equatorial to critical velocity (column 4), the polar and equatorial radii (columns 5 and 6), the mass (column 7), and the polar and equatorial temperatures (columns 8 and 9).

The first derived quantity is the projected rotational velocity $V \sin i$, which depends mainly on the adopted value of gravity exponent β. With larger β, the equatorial regions are darker and contribute less in the extreme line wings. Consequently, the best fits accommodate a slightly larger value of $V \sin i$ at the nominally accepted value of $\beta = 0.25$ compared to the case of no gravity darkening, $\beta = 0$. Fitting errors admit a range of ± 3 km s^{-1} in the derived $V \sin i$ value. We find, however, that the fits of Mg II λ4481 become much worse for models close to critical rotation, which confirms the inclination range of $60^\circ < i < 90^\circ$ found by Stoeckley & Buscombe (1987) based on similar profile studies. The estimates of stellar radii and mass are almost independent of the choice of i and β, and it is only the range in stellar temperature between the equator and pole that increases with β. Note, however, that the geometric mean of the equatorial and polar temperatures is almost the same in all the models, which results from matching the integrated K-band flux (reflecting the average temperature across the visible hemisphere). The internal errors of the fitting procedure (exclusive of any systematic errors associated with the model atmospheres and fluxes) lead to errors of $\pm 1\%$ in the radii and $\pm 7\%$ in mass.

4. Fits of Interferometric Visibility Using Physical Models

All of the models in Table 3 make acceptable fits of the spectroscopic data, and to further discriminate between them we turn to the model predictions about the interferometric visibilities. Here we discuss how to predict the visibility patterns associated with the physical models and how the observed visibilities can be used to evaluate the remaining parameters, in particular the inclination and the gravity darkening exponent. We first explore the goodness of fit for the full grid of models shown in Table 3 and we determine what parameter set minimizes the reduced chi-square for the whole set and subsets of the visibilities. We then compare the results with an independent approach based upon a guided search of the multi-parameter space.

We created K-band surface intensity images of the stellar disk for each case in Table 3 and made a two-dimensional Fourier transform of the image for comparison with the interferometric visibility (Domiciano de Souza et al. 2002). The modulus of the Fourier transform relative to that at frequency zero is then directly comparable to the observed visibility at a particular coordinate in the (u, v) spatial frequency plane (defined by the ratio of the projected baseline to the effective wavelength of the filter).

The predicted variation in visibility as a function of baseline is shown in Figure 8 for three selected models and for two orientations: the top set of three plotted lines corresponds to an interferometric baseline parallel to the polar (minor) axis while the lower set corresponds to the equatorial (major) axis. The CHARA Array observations correspond to baselines between 188 and 328 m, so we are sampling the main lobe of visibility. Model A corresponds to the case with $i = 90°$ and $\beta = 0.25$ (see Table 3). The visibility drops much more rapidly in the direction along the major axis compared to the minor axis, and consequently the variations in interferometric visibility in different directions in the (u, v) plane set the orientation of the star in the sky. Model B is also based on the nominal gravity darkening exponent value of $\beta = 0.25$, but the inclination is $i = 70°$ in this case. There are subtle differences in the pole to equator axis visibilities from model A that result from the greater rotational distortion and smaller polar radius in model B. Finally, model C shows the $i = 90°$ case but with no gravity darkening ($\beta = 0$). Now the equatorial flux is easily seen out to the extreme approaching and receding limbs, and the star appears larger in this dimension (resulting in lower visibility). These models show that although the differences due to stellar orientation in the sky are seen at all baselines, the smaller differences related to stellar inclination and gravity darkening are most apparent at longer baselines. Indeed, future observations with even longer baselines (or shorter wavelengths) that reach into the second lobe would strongly discriminate between these models.

We made a two-parameter fit to match the predicted and observed visibilities of Regulus. The first parameter is the position angle of the minor (rotation) axis in the sky α. The second parameter is an angular scaling factor, the ratio of best fit distance to the adopted distance from the *Hipparcos* parallax. In principle, the combination of the K-band flux and adopted temperature model leads to a predicted angular size (or stellar radius for a given distance), but the observed errors in absolute flux and distance will lead to a predicted angular size that may be marginally different from the actual angular size. The use of the scaling parameter provides a simple way to both check the prediction and adjust the spatial frequency scaling to best fit the observed visibilities. The results of these fits are given in Table 3 which lists the minor axis angular radius (column 10), major axis angular radius (column 11), the position angle α (column 12), the scaling factor $d/d(Hipparcos)$ (column 13), and the reduced chi-square of the fit χ^2_ν (column 14; for $N = 69$ measurements and $\nu = 2$ fitting parameters). We estimate that the errors in position angle are $\pm 2\overset{\circ}{.}8$ and in scaling factor are $\pm 1\%$ (based upon the increase in χ^2_ν with changes in these parameters). We see that the scaling factors are generally less than 2% different from unity, well within the error budget from the comparable errors in the estimates of the K-band flux, parallax, and effective wavelength of the CHARA K' filter.

The best overall fit is found for the rotational model with $i = 90°$ and $\beta = 0.25$, and

we show the predicted image of the stellar disk in the sky and its associated visibility in the (u, v) plane for this model in Figure 9. The upper part of the right panel shows the visibility as a gray-scale intensity and the polar axis as a dotted line (along the longer dimension in the visibility distribution). Black squares mark the positions in the (u, v) plane corresponding to the CHARA interferometric observations. The lower panel shows the point symmetric (u, v) plane, and there each observation is assigned a gray-scale intensity based upon the normalized residual, $(V_{\rm obs} - V_{\rm cal})/\sigma_V$. Note that the poor fits are the most apparent in this representation, but that there is no evidence of any systematic trends in the residuals with position in the (u, v) plane. The relative close proximity in the (u, v) plane of measurements that are above and below the predicted visibility suggests that the outstanding differences are due to measurement error rather than deficiencies in the models. The fact that the minimum chi-square is $\chi^2_\nu = 3.35$ rather than the expected value of unity indicates that our internal estimates of error in visibility (from the scatter within a sequence of fringe scans) may not adequately represent the total error budget. However, it is well known that the temporal power spectrum of atmospheric fluctuations has a steep slope. Since the calibration cycle has a much lower frequency than the scan to scan cycle, it is natural that the noise estimate from the latter underestimates the former.

We showed above in Figure 8 that the interferometric visibilities at all baselines provide a strong constraint on the position angle α, and we illustrate this striking dependence in Figure 10. This series of panels shows the normalized residuals from the model predictions for the $i = 90^\circ$ and $\beta = 0.25$ case as a function of baseline. The sky orientation of the K-band image of the star is shown to the right of each panel. The residuals for all baselines clearly obtain a well defined minimum for $\alpha = 85\overset{\circ}{.}5$ (*third panel from top*). Figure 11 shows the reduced chi-square as a function of α for both the entire set of measurements (*solid line*) and the long baseline measurements only ($B_{\rm proj} > 270$ m; *dotted line*). Both sets yield a consistent minimum, and the long baseline data are particularly sensitive to the position angle orientation.

The visibility constraints on the inclination and gravity darkening exponent are less pronounced but still of great interest. We show in Figure 12 the reduced chi-square as a function of the gravity darkening exponent β for a series of $i = 90^\circ$ model fits. The best fit occurs at $\beta = 0.25$ for the full set of observations, and this is also the value derived from gravity darkening studies of B-stars in eclipsing binary stars (Claret 2003). The formal 1σ error limit yields an acceptable range from $\beta = 0.12$ to 0.34, but $\beta = 0$ (no gravity darkening) can only be included if we extend the range to the 99% confidence level. However, recall from Figure 8 that most of the sensitivity to gravity darkening is only found at longer baselines and especially at those along the polar axis. Thus, we also show in Figure 12 the value of reduced chi-square for the $i = 90^\circ$ solutions in two subsets: measurements with baselines

greater than 270 m (31 points) and those with a position angle close to the polar axis orientation (6 points from MJD 53103.2 – 53104.2; see Table 1). Both sets (especially the latter, polar one) show much larger excursions and indicate β values close to 0.25. Note that we did not try models with $\beta > 0.35$ since such models have equatorial temperatures that are cooler than the lower limit of our flux grid. The most sensitive polar subset helps establish more practical error limits, and we adopt $\beta = 0.25 \pm 0.11$ as our best overall estimate. This analysis demonstrates that the inclusion of gravity darkening is key to fitting the CHARA data in the most sensitive part of the visibility curve.

The greater sensitivity of the long baseline and polar data is also apparent in the fits with differing inclination angle. We show in Figure 13 the run of reduced chi-square with inclination for models with $\beta = 0.25$. A shallow minimum at $i = 90°$ is found using all the data, but the same minimum is much more convincingly indicated in fits of the long baseline and polar data alone. The 1σ error limit of the latter sample admits a range of $78° - 90°$. Hutchings & Stoeckley (1977) also derived an inclination of $i = 90°$ for Regulus through a comparison of ultraviolet and optical photospheric line widths.

It is interesting to compare the rotation axis vector direction, determined here by combination of the angles i and α, with the space velocity vector direction. Hipparcos proper motion and parallax results (Perryman et al. 1997) combined with a new radial velocity value of $V = +7.4 \pm 2.0$ km s^{-1}, derived from the analysis described above of the Mg II λ4481 line, provide the necessary input for making this comparison. The angular values representing the space velocity that correspond to our measurements of $i = 90° \pm 15°$ and $\alpha = 85\overset{\circ}{.}5 \pm 2\overset{\circ}{.}8$ are $i_s = 75\overset{\circ}{.}2 \pm 4\overset{\circ}{.}0$ and $\alpha_s = 271\overset{\circ}{.}1 \pm 0\overset{\circ}{.}1$. Because α is inherently ambiguous by 180°, $\alpha - \alpha_s = -5\overset{\circ}{.}6 \pm 2\overset{\circ}{.}8$ and $i - i_s = 14\overset{\circ}{.}8 \pm 15\overset{\circ}{.}5$. This suggests that Regulus is moving very nearly pole-on through space.

We have checked these models through a comparison with an independent code based upon the scheme first outlined by van Belle et al. (2001), using a new generation of that code that conducts its comparisons in Fourier space rather than in image space. This method uses a different numerical realization of the geometry of the star, but one that is based on the same Roche approximation adopted above. There are six key parameters involved in this method (polar radius, i, α, β, rotation speed, and, albeit with low sensitivity, polar temperature) that define the projection of the stellar surface on the sky. This sky projection was then run through a two-dimensional Fourier transform, and a reduced chi-square was calculated from a comparison of the observed and model values for V^2. A multi-dimensional optimization code was then utilized to derive the best solution, a process that took typically 500 iterations (Press et al. 1992). The results are compared with those from fitting a uniform ellipsoid (§2.2) and from the spectroscopically constrained fits (Table 3) in Table 4. We

see that all three methods agree on the orientation of the polar axis in the sky, and both the grid search and spectroscopically constrained approaches find the same results for the angular sizes and inclination. The only discrepancy concerns the value of β, and the lower value derived from the grid search scheme is probably the result of the insensitivity to this parameter of the majority of the measurements in the whole sample. We place more reliance on the results of the sensitive polar sample in the spectroscopically constrained fit (Fig. 12).

In summary, we find that infrared interferometric measurements of Regulus over a wide range of position angle are consistent with parameters derived from spectroscopic criteria, and determine additional parameters which are not available from spectroscopy, particularly including the position angle of the rotation axis on the sky α, the inclination of that axis to the line of sight i, and the gravity darkening coefficient β. Our adopted results and their errors are summarized in Table 5. Our physical models for this rapidly rotating star indicate that Regulus has an equatorial radius that is 32% larger than the polar radius. Its rotation period is 15.9 hours, which corresponds to an equatorial rotation speed that is 86% of the critical break-up velocity. Fits of the CHARA observations require the presence of significant gravity darkening with an equatorial temperature that is only 67% of the polar temperature.

5. Conclusions

We have shown in a series of increasingly complex models, ultimately tied to physical parameters strongly constrained by spectroscopy, that Regulus exhibits features expected for a rapidly rotating star of its spectral type, namely oblateness and gravity darkening. Geometric fits to fringe visibility, first with discrete position angle determinations of uniform disk diameters and then with an ellipsoidal model, clearly show the marked rotational oblateness of the star. When we couple the visibilities to models that incorporate parameters to which high resolution spectroscopy is sensitive, we find mutual consistency between the interferometric and spectroscopic results. Indeed, we believe that the combination of these complementary astrophysical probes - interferometry and spectroscopy - provides the best means for exploiting new high spatial resolution measurements from such instruments as the CHARA Array.

Our observations provide the first interferometric evidence of gravity darkening in rapidly rotating stars. Furthermore, the CHARA Array results offer the first claim of gravity darkening in a star that is not a known member of an eclipsing binary system (Claret 2003). The agreement between the measurement of the angular diameter from the CHARA visibilities and that based upon the K-band flux provides an independent verification of the infrared flux method for estimating angular diameters first introduced by Blackwell & Shallis

(1977), and it indicates that the B-star fluxes predicted by line blanketed, LTE atmospheres models by R. L. Kurucz agree with the observed angular diameter and infrared flux within the observed errors.

New interferometric observations of this kind offer the means to determine how close the most rapidly rotating stars are to their critical rotation speeds, and this may help solve the longstanding problem of the nature of mass loss in the rapidly rotating Be stars, for example (Porter & Rivinius 2003). These observations may also finally allow us to test models of interior structure and evolution for massive rotating stars (Endal & Sofia 1979; Heger & Langer 2000; Meynet & Maeder 2000). We show in Figure 14 the position of Regulus in the theoretical Hertzsprung-Russell diagram based upon the surface integration of σT^4 to estimate the luminosity and upon an average temperature derived from the luminosity and surface area of our best-fit model. We also show the zero-age to terminal-age main sequence evolutionary paths for non-rotating 3 and $4M_{\odot}$ stars based upon the work of Schaller et al. (1992). The shaded region represents the main sequence evolutionary parameters for a star with the mass and errors in mass we derive from the joint spectroscopic-interferometric analysis. The position of Regulus in this diagram shows that the star is overluminous for its mass as predicted for rotating stars that evolve to higher luminosity as fresh H is mixed into their convective cores (Heger & Langer 2000; Meynet & Maeder 2000). If Regulus is placed on an isochrone without consideration of this excess luminosity, the age of the star is overestimated. This is the likely explanation for the apparent discordance in age that has been noted for the α Leo A and B components (Gerbaldi et al. 2001). The new era of long baseline interferometry offers us the means to probe the evolution of rotating stars as has never before been possible.

6. Acknowledgements

This research has been supported by National Science Foundation grants AST–0205297 and AST–0307562. Additional support has been received from the Research Program Enhancement program administered by the Vice President for Research at Georgia State University. Portions of this work were performed at the California Institute of Technology under contract with the National Aeronautics and Space Administration. We thank CHARA Array Operator P. J. Goldfinger for her care in obtaining many of these observations.

As this is the first scientific paper from the CHARA Array, a project whose origin dates back to the formal establishment of CHARA at Georgia State University in 1984, it is appropriate to acknowledge the many individuals and organizations responsible for bringing the dream of this facility into reality. The College of Arts and Sciences has generously

supported CHARA from its conceptual beginnings in 1983 when Dean Clyde Faulkner agreed to establish a research center with the goal of building a facility for high angular resolution astronomy. The present Dean, Lauren Adamson, graciously continues to support the center in increasingly difficult financial times. Georgia State President Carl Patton has been an enthusiastic supporter of CHARA, having visited the Array site on numerous occasions. Tom Lewis, Vice President for External Affairs, has often accompanied President Patton to California and has been a strong proponent for the project. We are particularly indebted to Cleon Arrington, former Vice President for Research and Sponsored Programs, who worked with tireless enthusiasm with the CHARA director to raise matching funds to build the Array. The exceptional nurturing and substantial backing given by the administration of Georgia State University is deeply appreciated.

We also wish to acknowledge the continuing support provided by administrative service elements of the University during the years of construction of the Array. We particularly thank Albertha Barrett, now Assistant Vice President for Research, and her staff in research administration for their patience and expertise in dealing with grants and contracts related matters. This project has involved thousands of procurements, and we acknowledge David Bennett, Larry McCalop, and Howard Hopwood of the University's purchasing department for their exceptional efforts to ensure that CHARA got what it needed when it needed it. The expertise of Charles Hopper, manager of the physics and astronomy shop, has been critical to the materialization of the hundreds of custom designed and fabricated parts that comprise the many subsystems of the Array. CHARA Site Manager Bob Cadman has ably served as our first line of defense on any number of matters, from groundbreaking to the present time. Finally, the devotion of Alexandra "Sandy" Land, CHARA's Business Manager, has been a key ingredient to seeing this effort finished on schedule and within budget.

The National Science Foundation has provided substantial funding for preliminary and detailed design and ultimately for construction of the CHARA Array through NSF grant AST–9414449. The kind support and careful oversight provided by Wayne Van Citters, Kurt Weiler, Benjamin Snavely, and James Breckinridge, successive directors of the Advanced Technology and Instrumentation Program, is gratefully acknowledged.

The W. M. Keck Foundation provided funding to expand the Array from a five- to a six-telescope instrument and to enhance our beam combining capability. We thank Maria Pellegrini and Mercedes Talley of the Keck Foundation for making this support possible.

We thank Kenneth Ford of the David and Lucile Packard Foundation for his role in providing funds that capped the University's matching obligation to the NSF.

Jack Kelly, Georgia State physics alumnus, kindly donated funds in support of an exhibit

hall attached to CHARA's main operations building on Mount Wilson.

Several individuals worked closely with CHARA during the planning and design years, and we acknowledge the valuable contributions made by Allen Garrison and William Robinson of the Georgia Tech Research Institute and also by William Hartkopf, our colleague for many years at Georgia State who now continues CHARA's original tradition of binary star speckle interferometry at the U.S. Naval Observatory.

We thank Robert Jastrow, former director of the Mount Wilson Institute, for inviting us to explore Mount Wilson as a possible site for the CHARA Array and for assisting in many ways to ease the complications of obtaining site access. Once on Mount Wilson, we were fortunate to have the services of Eric Simison, president of Sea West Enterprises, who became not only our prime contractor but also a core member of our design and engineering team. We also acknowledge Terry Ellis, former District Ranger for the Angeles River Ranger District of the Angeles National Forest for his kind guidance in our efforts to fulfill NEPA and Department of Agriculture guidelines in locating on Mount Wilson.

Ingemar Furenlid served on the astronomy faculty at Georgia State from 1982 until he passed away on 1994 February 11. He was a respected colleague and dear friend to several of us and at all times a hearty cheerleader for CHARA. We deeply regret that he is not among the co-authors of this publication, and we dedicate this first CHARA Array paper to his memory.

REFERENCES

Abt, H. A., & Biggs, E. S. 1972, Bibliograpy of Stellar Radial Velocities (New York: Latham Process Corp.)

Abt, H. A., Levato, H., & Grosso, M. 2002, ApJ, 573, 359

Alekseeva, G. A., et al. 1996, Baltic Astron., 5, 603

Barry, D. J., Bagnuolo, W. G., Jr., & Riddle, R. L. 2002, PASP, 114, 198

Benson, J. A., Dyck, H. M., & Howell, R. R. 1995, Appl. Opt., 34, 51

Berg, R. A. 1970, Ph.D. dissertation, Univ. Virginia

Blackwell, D. E., & Shallis, M. J. 1977, MNRAS, 180, 177

Le Borgne, J.-F., et al. 2003, A&A, 402, 433

Born, M., & Wolf, E. 1999, Principles of Optics: Electromagnetic Theory of Propagation, Interference and Diffraction of Light (7th ed.) (Cambridge: Cambridge Univ. Press)

Bouchet, P., Schmider, F. X., & Manfroid, J. 1991, A&AS, 91, 409

ten Brummelaar, T., et al. 2004, submitted to ApJ

Claret, A. 2003, A&A, 406, 623

Code, A. D., Davis, J., Bless, R. C., & Hanbury Brown, R. 1976, ApJ, 203, 417

Cohen, M., Walker, R. G., Barlow, M. J., & Deacon, J. R. 1992, AJ, 104, 1650

Collins, G. W., II, Truax, R, J., & Cranmer, S. R. 1991, ApJS, 77, 541

Cutri, R. M., et al. 2003, The 2MASS All-Sky Catalog of Point Sources (Pasadena: IPAC and Univ. Mass.)

Domiciano de Souza, A., Kervella, P., Jankov, S., Abe, L., Vakili, F., di Folco, E., & Paresce, F. 2003, A&A, 407, L47

Domiciano de Souza, A., Vakili, F., Jankov, S., Janot-Pacheco, E., & Abe, L. 2002, A&A, 393, 345

Elvey, C. T. 1930, MNRAS, 89, 222

Endal, A. S., & Sofia, S. 1979, ApJ, 232, 531

Fitzpatrick, E. L. 1999, PASP, 111, 63

Gezari, D.Y., Schmitz, M., Pitts, P.S., & Meade, J. M. 1993, Catalog of Infrared Observations, NASA Reference Publ. 1294 (Washington, DC: NASA)

Gerbaldi, M., Faraggiana, R., & Balin, N. 2001, A&A, 379, 162

Gray, R. O., Corbally, C. J., Garrison, R. F., McFadden, M. T., & Robinson, P. E. 2003, AJ, 126, 2048

Hanbury Brown, R. 1968, ARA&A, 6, 13

Hanbury Brown, R., Davis, J., & Allen, L. R. 1974, MNRAS, 167, 121

Hanbury Brown, R., Davis, J., Allen, L. R., & Rome, J. M., 1967, MNRAS, 137, 393

Heger, A., & Langer, N. 2000, ApJ, 544, 1016

Henry, G. W., Fekel, F. C., Henry, S. M., & Hall, D. S. 2000, ApJS, 130, 201

Hoffleit, D. 1982, The Bright Star Catalogue (New Haven: Yale Univ. Obs.)

Hutchings, J. B., & Stoeckley, T. R. 1977, PASP, 89, 19

Johnson, H. L., & Morgan, W. W. 1953, ApJ, 117, 313

Johnston, I. D., & Wareing, N. C. 1970, MNRAS, 147, 47

Lanz, T., & Hubeny, I. 2003, ApJS, 146, 417

Maunder, E. W. 1892, The Observatory, 15, 393

McAlister, H. A., Mason, B. D., Hartkopf, W. I., & Shara, M. M. 1993, AJ, 106, 1639

McAlister, H. A., et al. 2004, Publ. SPIE, 5491, 472

Meynet, G., & Maeder, A. 2000, A&A, 361, 101

Morales, C., et al. 2001, ApJ, 552, 278

Norris, J. 1971, ApJS, 23, 213

Pauls, T. A., Young, J. S., Cotton, W. D., & Monnier, J. D. 2004, Publ. SPIE, 5491, 1231

Pickles, A. J. 1998, PASP, 110, 863

Perryman, M. A. C., et al. 1997, A&A, 323, 49

Porter, J. M., & Rivinius, T. 2003, PASP, 115, 1153

Press, W.H., Teukolsky, S. A., Vetterling, W. T., & Flannery, B. P. 1992, Numerical Recipes in C (Port Chester: Cambridge Univ. Press)

Radick, R. 1981, AJ, 86, 1685

Ridgway, S. T., Jacoby, G. H., Joyce, R. R., Seigel, M. J., & Wells, D. C. 1982, AJ, 87, 680

Schaller, G., Schaerer, D., Meynet, G., & Maeder, A. 1992, A&AS, 96, 269

Shajn, G., & Struve, O. 1929, ApJ, 71, 221

Singh, M. 1982, IBVS, 2188, 1

Slettebak, A. 1949, ApJ, 110, 498

Slettebak, A. 1963, ApJ, 138, 118

Slettebak, A. 1966, ApJ, 145, 126

Slettebak, A., & Reynolds, R. C. 1978, ApJS, 38, 205

Smith, K. C., & Dworetsky, M. M. 1993, A&A, 274, 335

Stee, Ph., & Bittar, J. 2001, A&A, 367, 532

Štefl, S., Hummel, W., & Rivinius, Th. 2000, A&A, 358, 208

Stoeckley, T. R., Carroll, R. W., & Miller, R. D. 1984, MNRAS, 208, 459

Stoeckley, T. R., & Buscombe, W. 1987, MNRAS, 227, 801

Sturmann, J., ten Brummelaar, T. A., Ridgway, S. T., Shure, M. A., Safizadeh, N., Sturmann, L., Turner, N. H., & McAlister, H. A. 2002, Publ. SPIE, 4828, 1208

Townsend, R. H. D., Owocki, S. P., & Howarth, I. D. 2004, MNRAS, 350, 189

Traub, W. A. 2000, in Principles of Long Baseline Stellar Interferometry, JPL Publ. 00-009, ed. P. R. Lawson (Pasadena: JPL)

Valdes, F., Gupta, R., Rose, J. A., Singh, H. P., & Bell, D. J. 2004, ApJS, 152, 251

van Belle, G. T., Ciardi, D. R., Thompson, R. R., Akeson, R. L., & Lada, E. A. 2001, ApJ, 559, 1155

von Zeipel, H. 1924, MNRAS, 84, 665

Wade, R. A., & Rucinski, S. M. 1985, A&AS, 60, 471

Wilson, R. E. 1963, General Catalogue of Stellar Radial Velocities (Washington, DC: CIW)

This preprint was prepared with the AAS LaTeX macros v5.2.

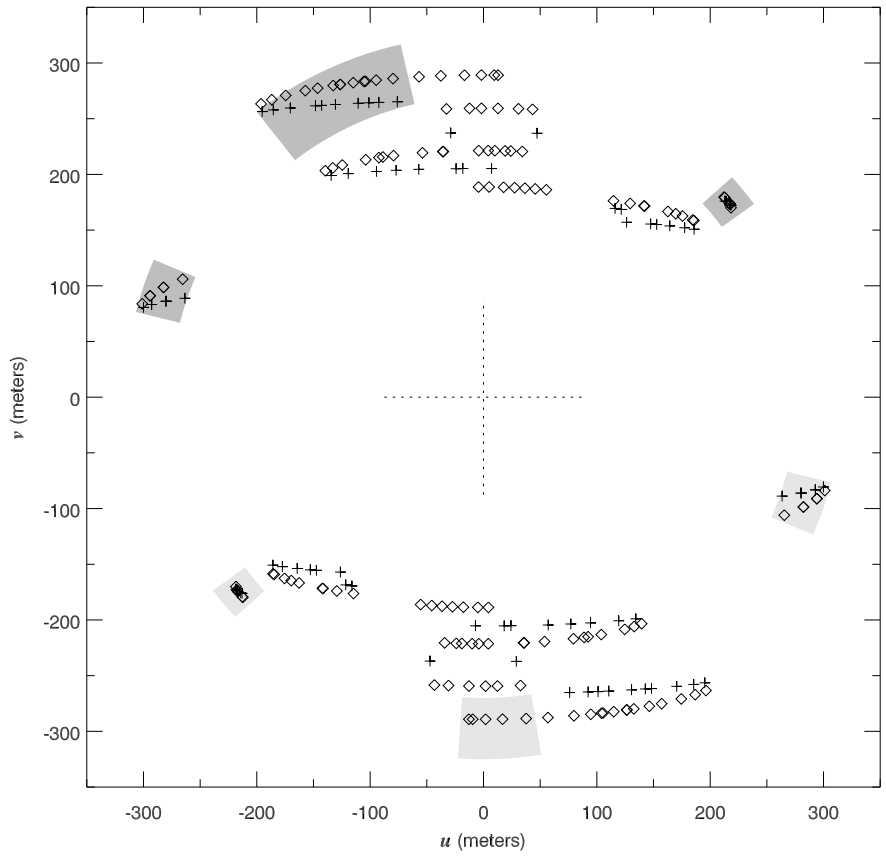

Fig. 1.— The baseline coverages for Regulus (*open diamonds*) and the check star HD 88547 (*plus signs*) are shown in the (u, v) plane above. The lighter shaded regions in the lower half indicate those measurements of Regulus used for a position angle dependent estimate of diameter (see Fig. 3), while the darker shaded regions in the upper half show the same for measurements of the check star.

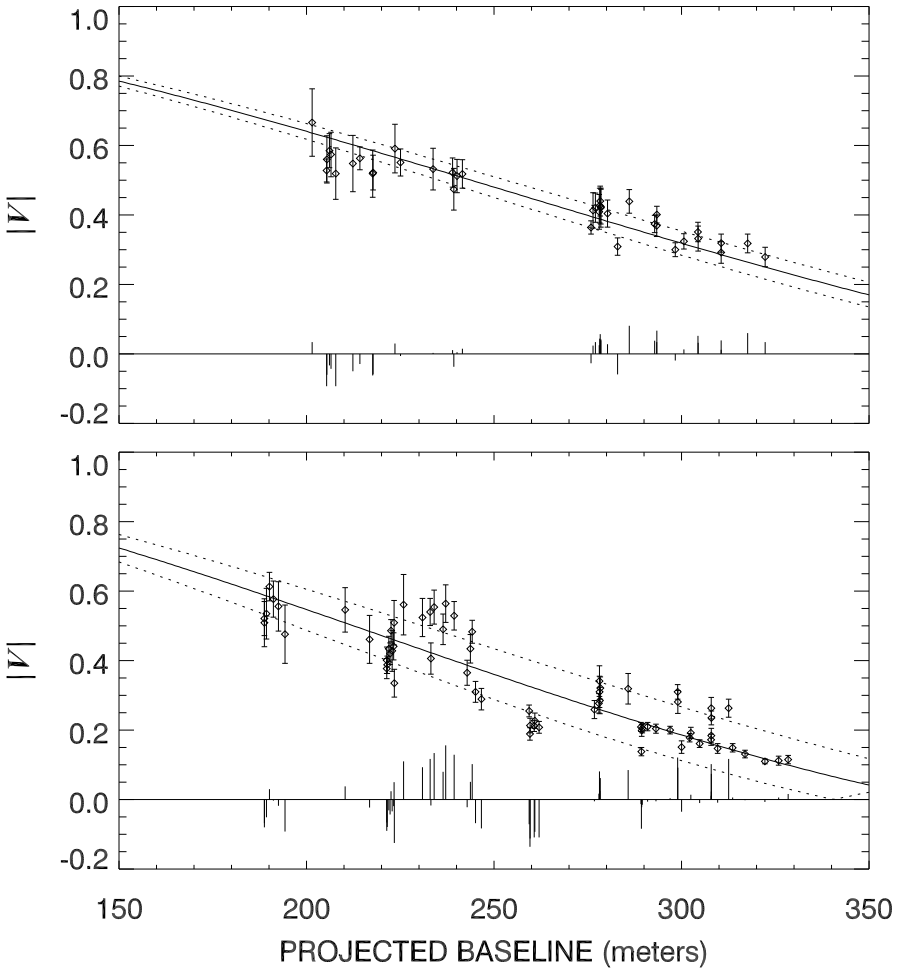

Fig. 2.— The best-fit uniform disk diameter fits to the calibrated visibilities are shown for the check star HD 88547 (*top panel*) and Regulus (*bottom panel*). The data for Regulus are clearly poorly fit by a uniform disk model.

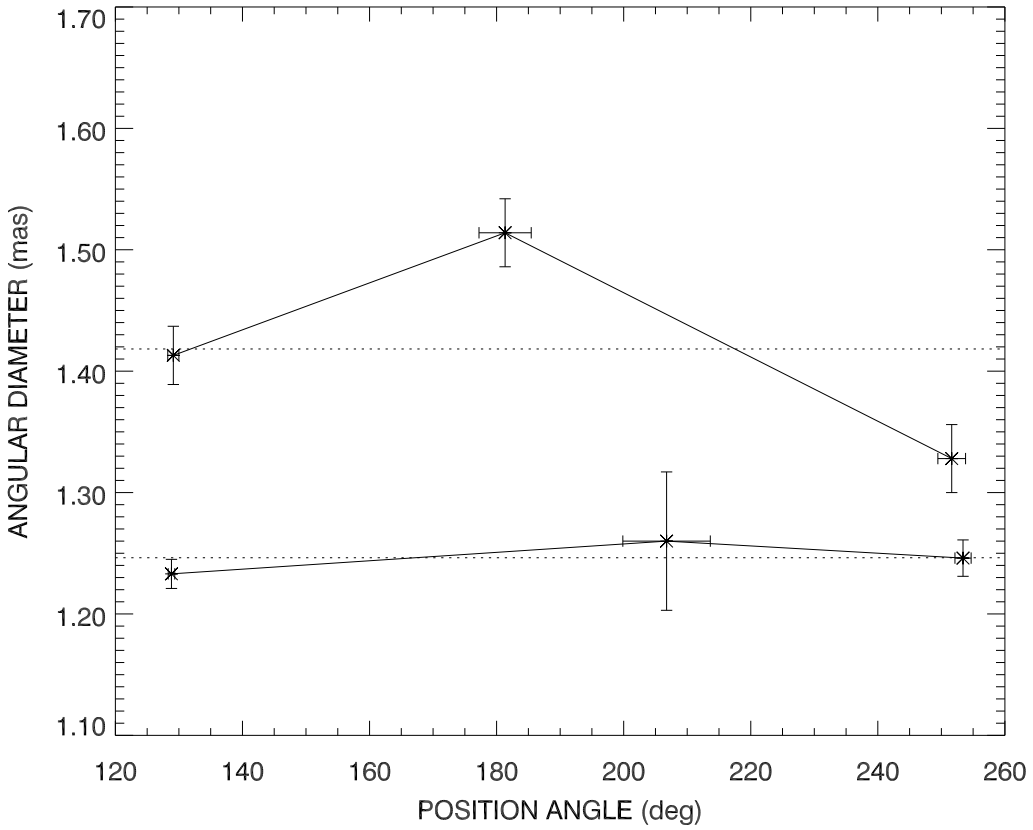

Fig. 3.— Uniform disk diameters calculated from the longest baseline data in the vicinity of three position angles indicated in Fig. 1 are shown for the check star HD 88547 (*lower values*) and Regulus (*upper values*). The dotted lines show the respective mean values of these 3 sets in each case. These results imply that the check star is round while Regulus is not.

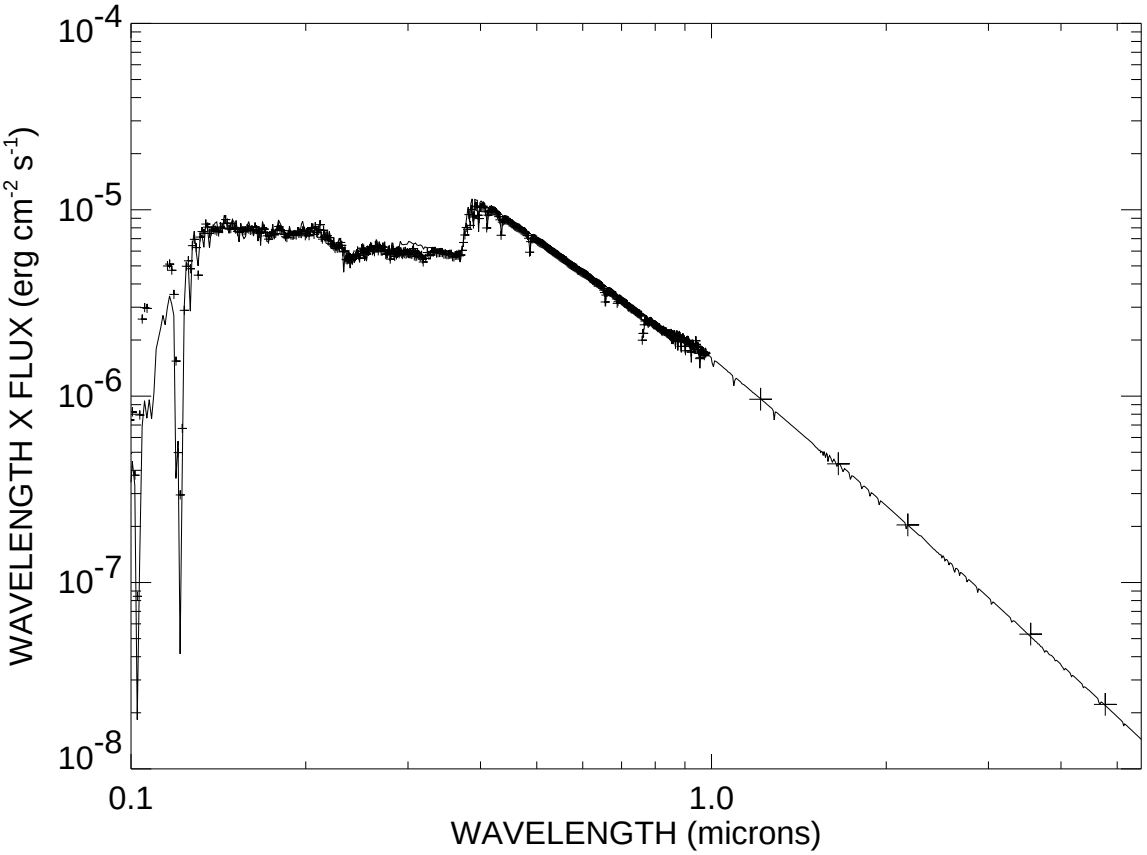

Fig. 4.— The full spectral flux distribution of Regulus. Smaller plus signs indicate the short wavelength observations which are binned to the same resolution as the model distribution (*solid line*) while the larger plus signs indicate fluxes from infrared magnitudes.

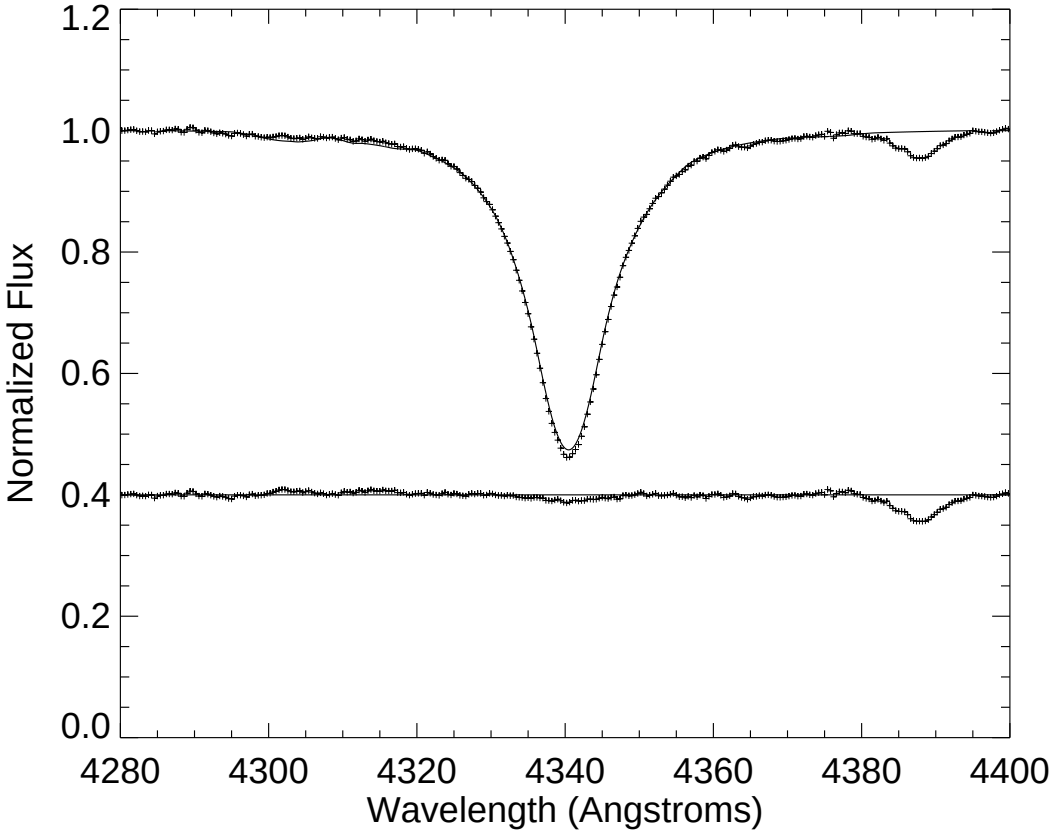

Fig. 5.— The observed (*plus signs*) and model (*solid line*) profiles for Hγ in the spectrum of Regulus. The plot corresponds to a model with a gravity darkening exponent $\beta = 0.25$ and an inclination $i = 90°$. The lower plot shows the residuals from the fit (note that the He I λ4387 line that was not included in the calculation).

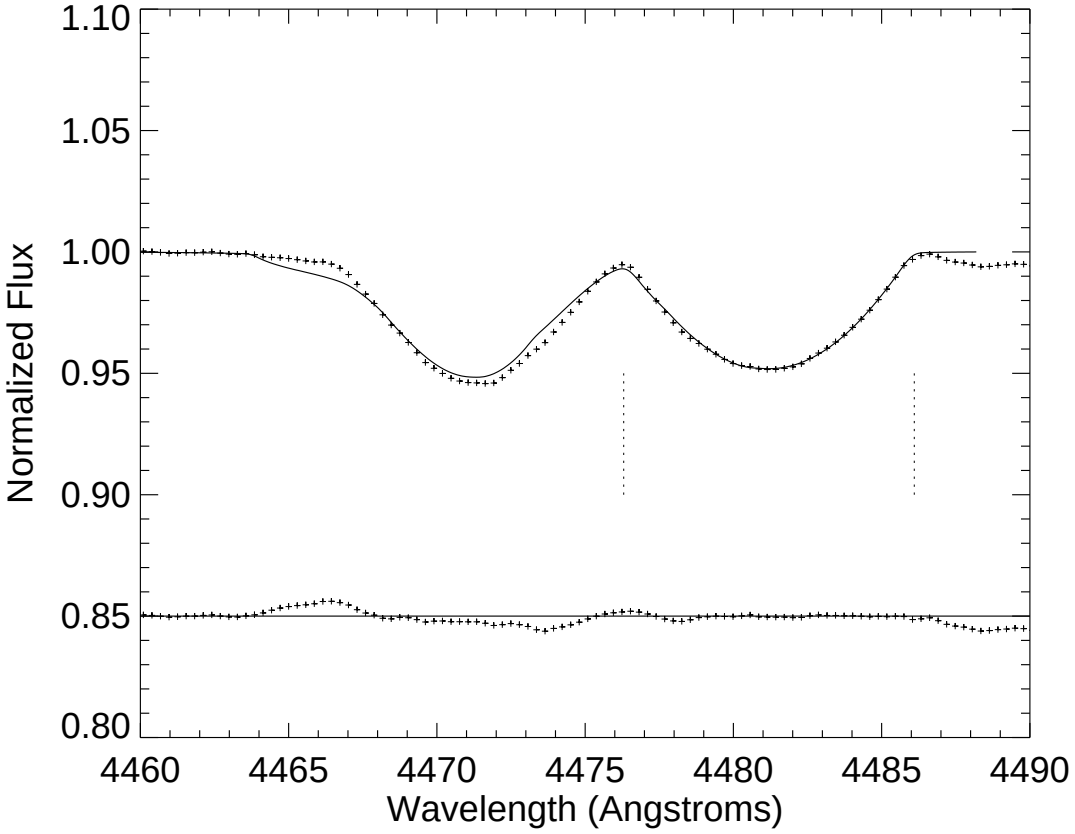

Fig. 6.— The observed (*plus signs*) and model (*solid line*) profiles for Mg II λ4481 in the spectrum of Regulus. The plot corresponds to a model with $i = 90°$ and $\beta = 0.25$. Residuals from the fit are shown below. Note that the He I λ4471 line and other weaker lines were not included in the fit of projected rotational velocity (which was based on the interval between the two vertical dashed lines.)

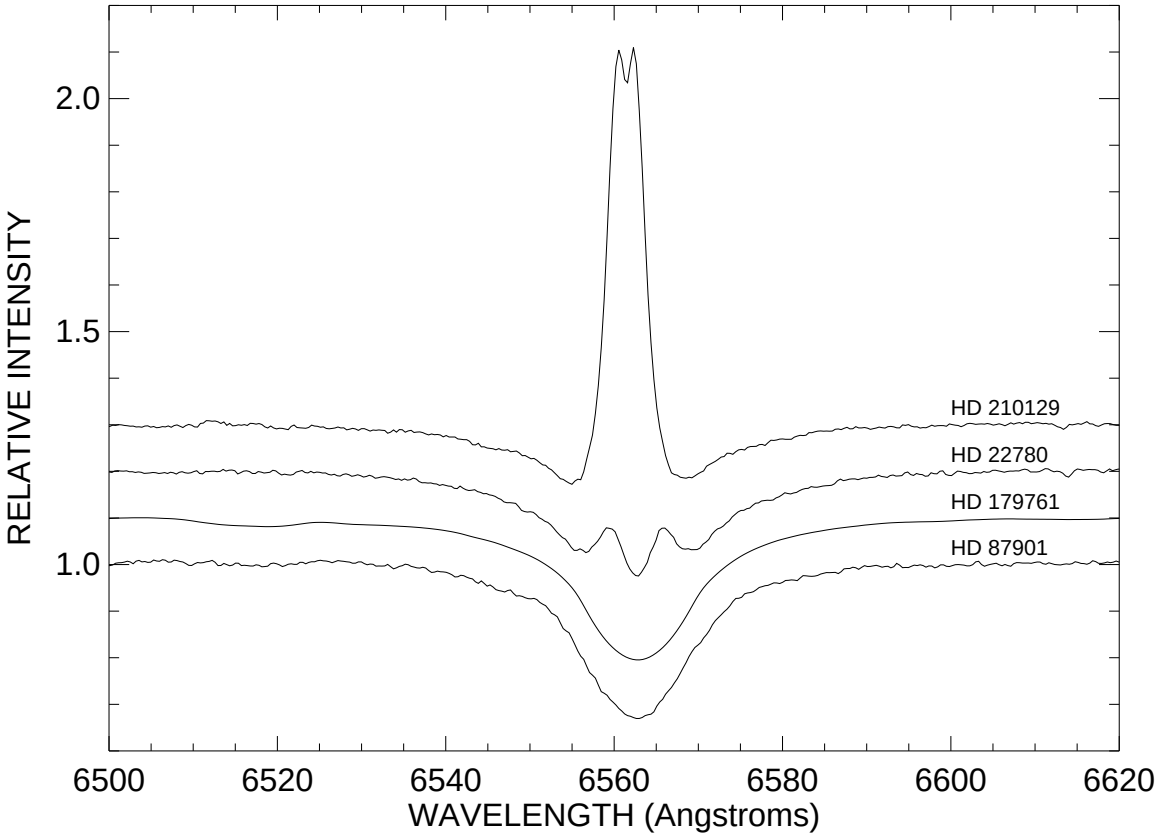

Fig. 7.— A plot of the Hα profile in the spectrum of Regulus (*bottom*; HD 87901). This is an average of eleven spectra made with the KPNO Coudé Feed Telescope from 2004 October 13 – 16. There is no evidence of the kind of disk Hα emission that is observed in rapidly rotating Be stars such as HD 22780 (*second from top*; B7 Vne) and HD 210129 (*top*; B7 Vne). Also shown is the photospheric Hα profile of the slowly rotating star HD 179761 (*third from top*; B8 II-III), which we artificially broadened to match the rotational broadening of Regulus. The close agreement between the photospheric line of HD 179761 and that of Regulus indicates that no disk emission is present.

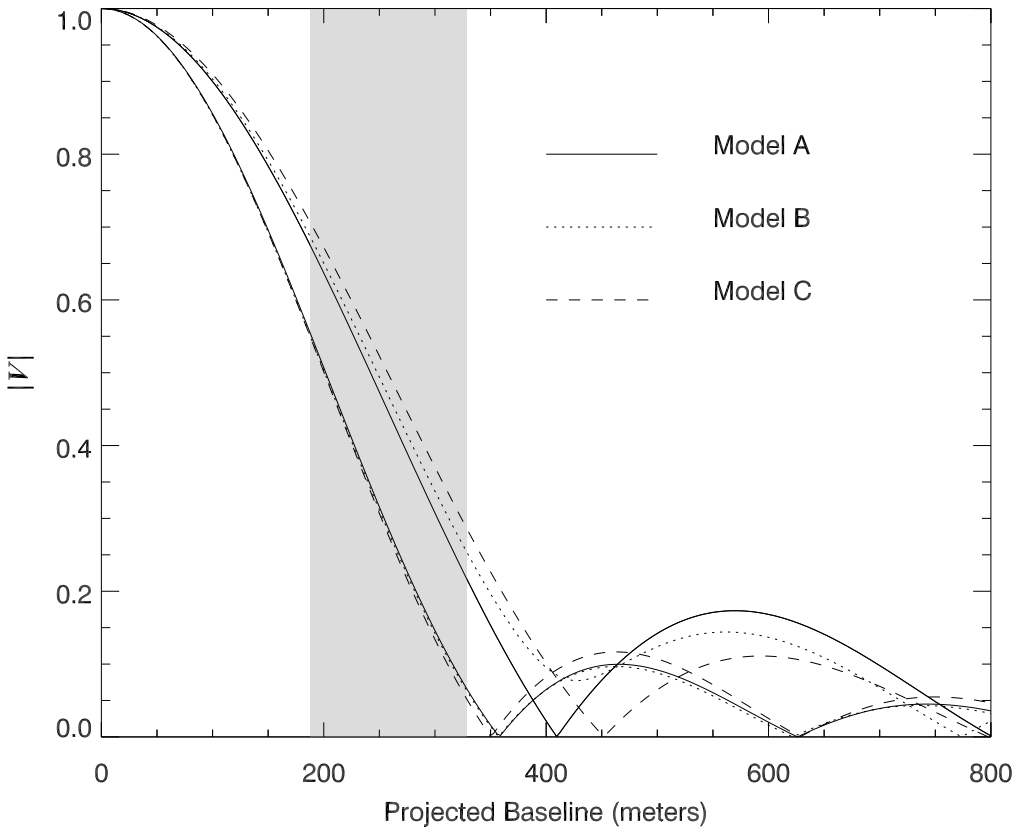

Fig. 8.— Predicted visibility variations with baseline for three rotation models and two sky orientations. The upper group corresponds to a baseline parallel to the minor (rotational) axis in the sky while the lower group corresponds to a baseline parallel to the major axis. The visibility curves are shown for the cases of $i = 90°, \beta = 0.25$ (**A**; *solid lines*), $i = 70°, \beta = 0.25$ (**B**; *dotted lines*), and $i = 90°, \beta = 0$ (**C**; *dashed lines*). The spatial frequency for a given baseline is shown for a filter effective wavelength of 2.1501 μm. The shaded region indicates the baseline range of the CHARA Array observations.

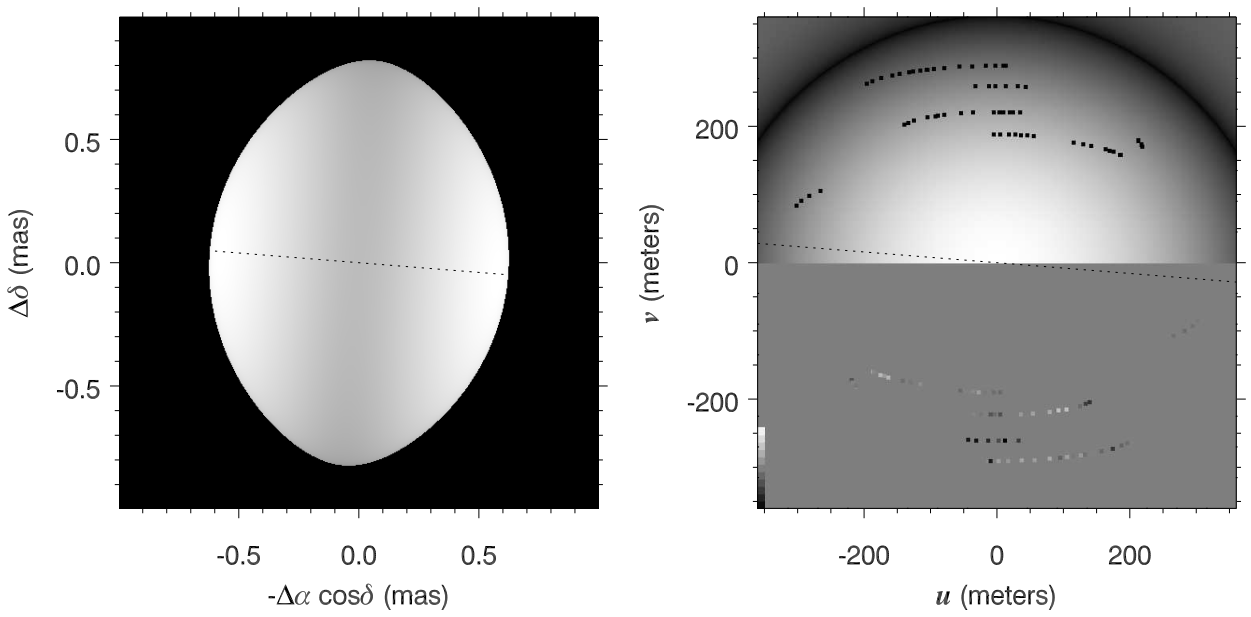

Fig. 9.— A K-band image of the star in the sky (*left*) and its associated Fourier transform visibility pattern in the (u, v) plane (*right*). In both cases north is at the top and east is to the left. The dotted, black line indicates the direction of the rotational axis for this $i = 90°$, $\beta = 0.25$, and $\alpha = 85\overset{\circ}{.}5$ model. The upper panel of the visibility figure (*right*) shows a grayscale representation of the visibility and the positions of the CHARA measurements (*black squares*). The lower panel shows the normalized residuals from the fit as a gray scale intensity square against a gray background in a point symmetric representation of the (u, v) plane. The legend at lower left shows the intensities corresponding to normalized residuals from -5 (*black*) to $+5$ (*white*). Note that the best fit points appear gray and merge with the background.

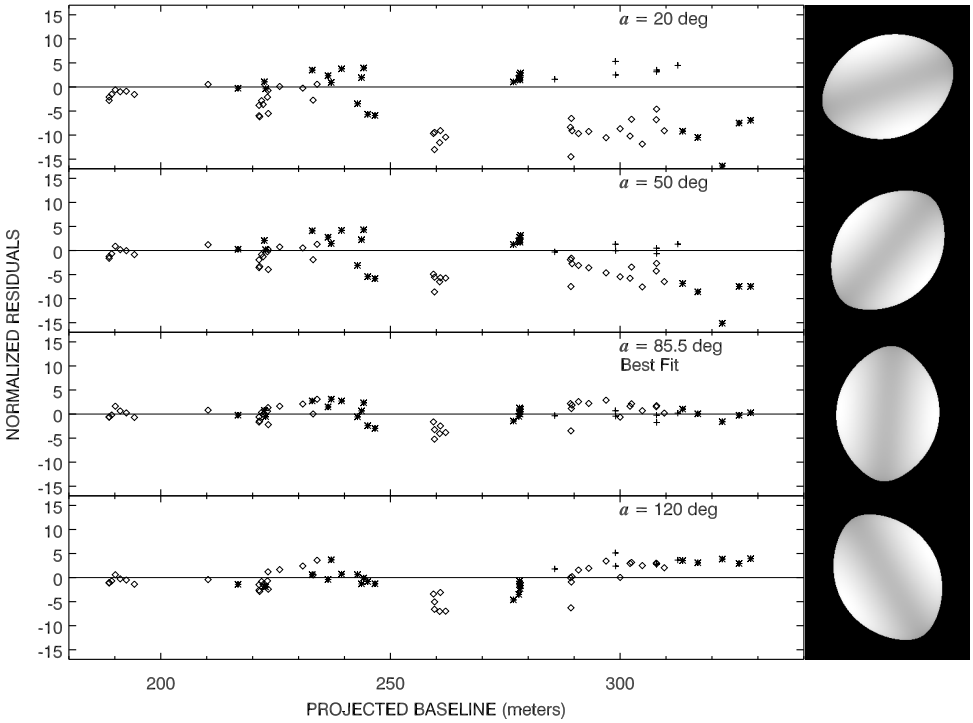

Fig. 10.— Normalized visibility residuals as a function of baseline. Each panel shows the residuals for the model star with $i = 90°$, $\beta = 0.25$, and a position angle α as indicated (and illustrated at right). The residuals are clearly minimized at the best fit value of $\alpha = 85\overset{\circ}{.}5$ (*third panel from top*). Plus signs indicate measurements in the (u, v) plane within 30° of the rotation axis (6 points), diamonds indicate those within 30° of the equator (40 points), and asterisks indicate the others at intermediate angles (23 points).

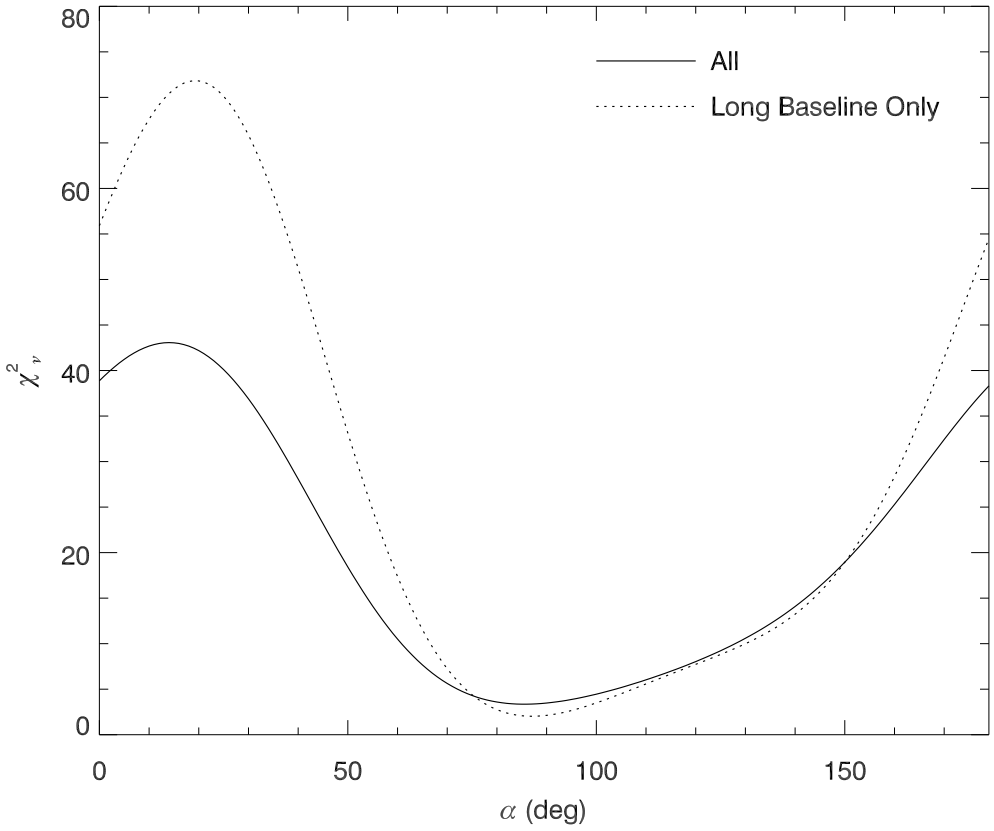

Fig. 11.— A plot of the reduced chi-square χ^2_ν of the visibility fits as a function of position angle α (for $i = 90°$ and $\beta = 0.25$). The solid line shows the reduced chi-square for whole sample while the dotted line shows the same for the long baseline data only.

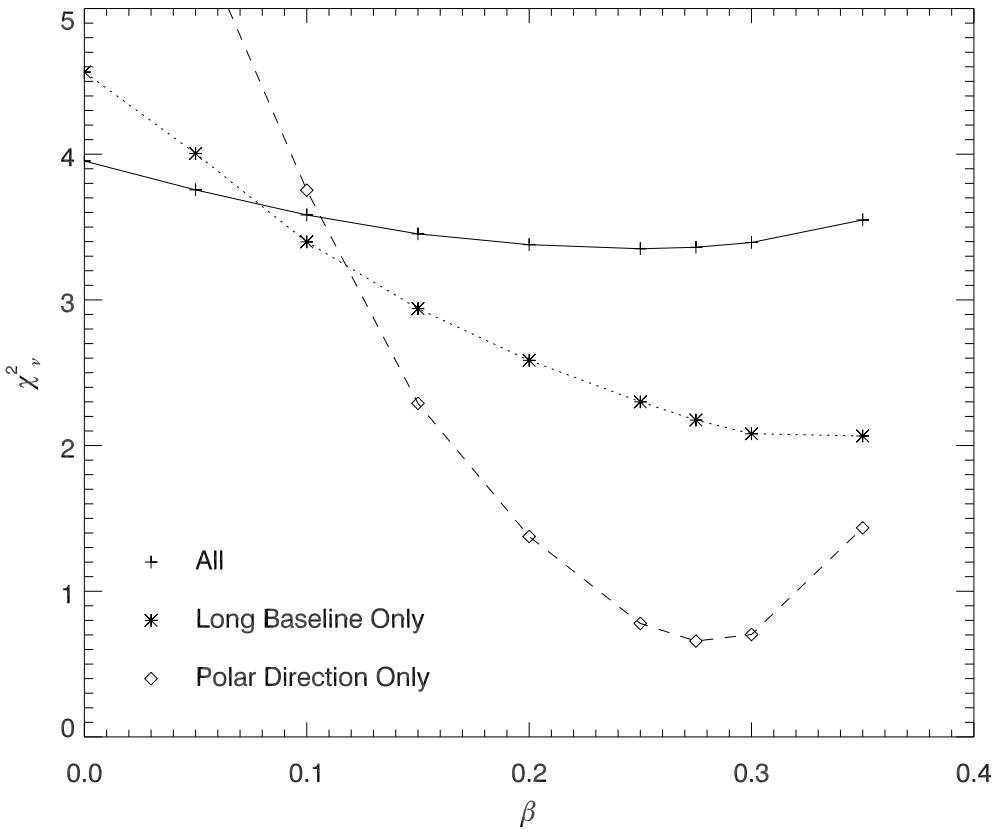

Fig. 12.— A plot of the reduced chi-square χ^2_ν of the visibility fits as a function of gravity darkening exponent β (for $i = 90°$). The solid line shows the reduced chi-square for whole sample (69 points). The dotted line shows the reduced chi-square of the same fits for the long baseline data only (31 points) while the dashed line shows the same for those long baseline data with a position angle near the orientation of the polar axis (the 6 points most sensitive to the selection of β). All these samples indicate a gravity darkening exponent near the predicted value of $\beta = 0.25$.

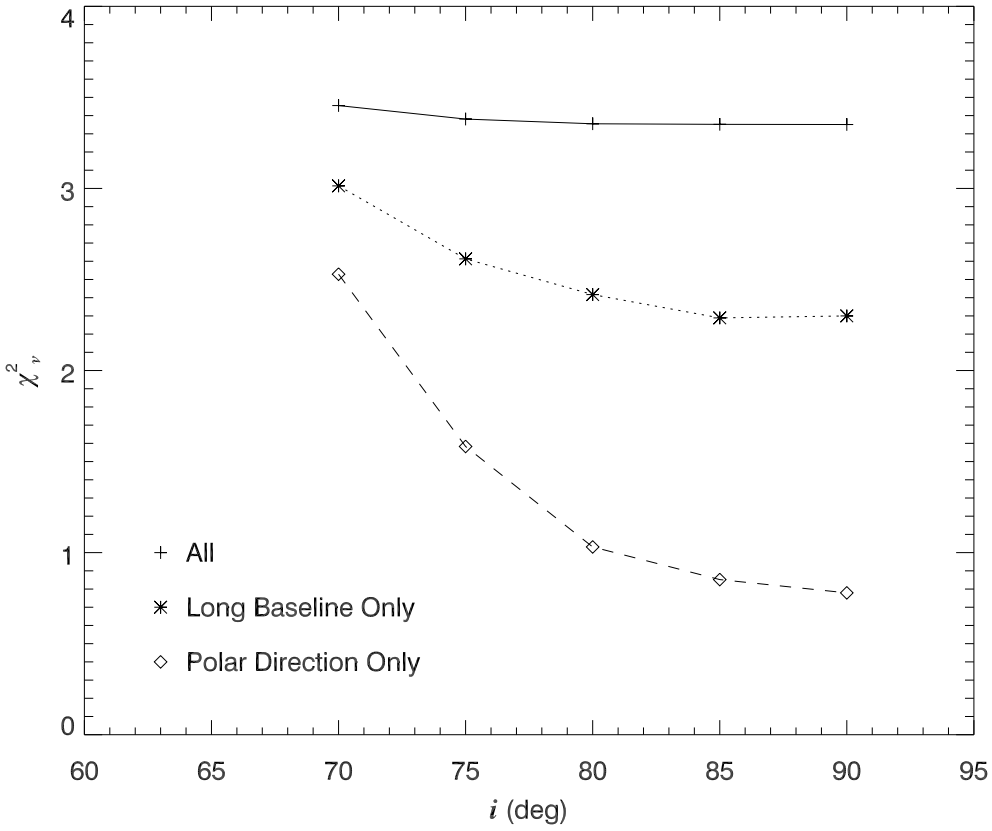

Fig. 13.— A plot of the reduced chi-square χ^2_ν of the visibility fits as a function of the rotation axis inclination angle i (for $\beta = 0.25$). The different lines correspond to the same samples as shown in Fig. 12.

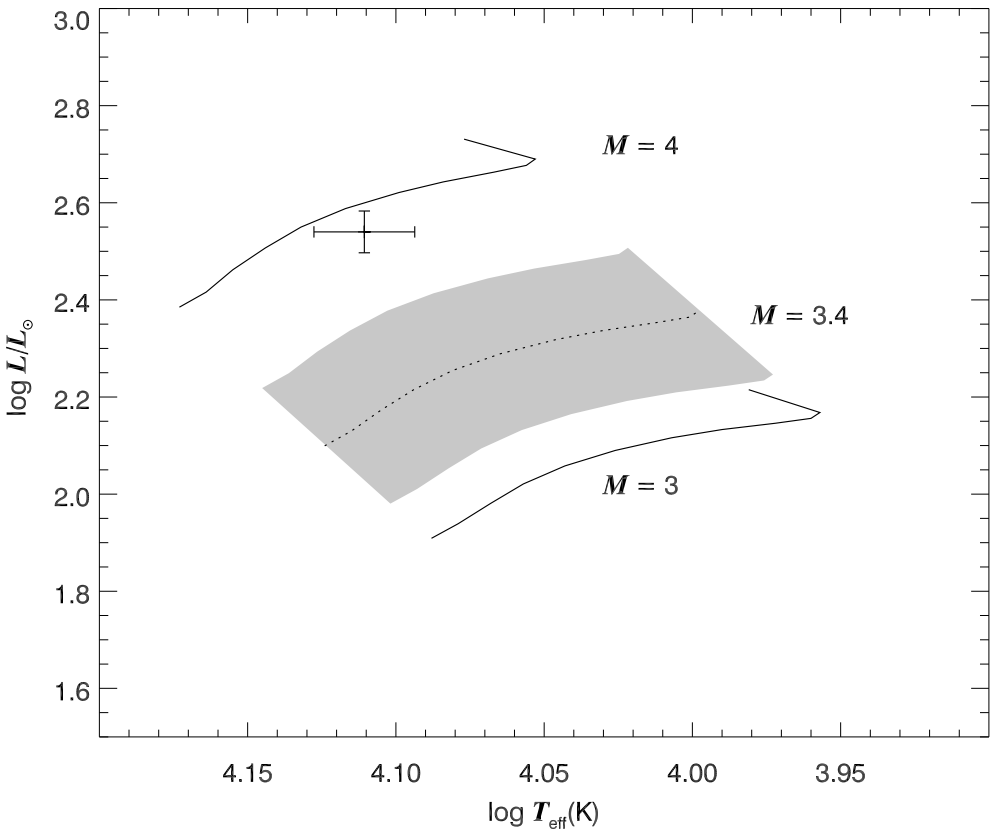

Fig. 14.— The Hertzsprung-Russell diagram for Regulus. The two solid lines show the track from zero age to terminal age main sequence (*left to right*) for non-rotating stars with initial masses of 3 and $4M_{\odot}$ (Schaller et al. 1992), while the dotted line and surrounding shaded area show the predicted region for a non-rotating star with the derived mass of Regulus and its associated error. The single point at $L/L_{\odot} = 347$ and $< T_{\rm eff} >= 12901$ K (from a surface integration of our numerical model) is well above the predicted position, indicating that the star is overluminous for its mass in comparison to models for non-rotating stars.

Table 1. Interferometric Measurements of Regulus (HD 87901)

MJD	Projected Baseline (m)	Baseline Position Angle (deg)	Calibrated Visibility
53074.188	188.76	181.33	0.520 ± 0.049
53074.200	188.77	178.49	0.508 ± 0.069
53074.215	189.31	174.62	0.535 ± 0.073
53074.227	190.11	171.71	0.613 ± 0.041
53074.238	191.17	168.98	0.576 ± 0.052
53074.250	192.51	166.29	0.556 ± 0.071
53074.263	194.26	163.41	0.476 ± 0.084
53078.237	222.54	140.50	0.486 ± 0.032
53078.262	232.97	135.70	0.539 ± 0.039
53078.280	239.36	132.82	0.528 ± 0.041
53078.297	244.18	130.51	0.483 ± 0.033
53079.207	210.30	146.95	0.546 ± 0.063
53079.222	216.82	143.36	0.461 ± 0.069
53079.235	222.84	140.36	0.427 ± 0.059
53079.269	236.42	134.15	0.490 ± 0.044
53080.250	233.17	202.38	0.405 ± 0.045
53080.309	223.41	189.25	0.334 ± 0.040
53080.351	221.40	178.92	0.400 ± 0.038
53080.366	221.95	175.06	0.433 ± 0.036
53080.382	223.23	171.17	0.440 ± 0.039
53081.167	246.64	214.46	0.289 ± 0.031
53081.181	245.06	212.86	0.310 ± 0.030
53081.196	242.83	210.87	0.365 ± 0.036
53081.228	237.11	206.00	0.563 ± 0.054
53081.243	234.04	203.22	0.553 ± 0.048
53081.259	230.92	200.10	0.524 ± 0.054
53081.288	225.89	193.79	0.560 ± 0.087
53081.307	223.35	189.13	0.509 ± 0.064
53081.339	221.40	181.09	0.376 ± 0.029
53081.354	221.53	177.40	0.387 ± 0.025
53081.368	222.29	173.79	0.420 ± 0.031
53088.224	313.63	207.81	0.148 ± 0.012
53088.243	307.88	204.22	0.172 ± 0.016
53088.262	302.17	200.16	0.178 ± 0.012
53088.281	296.95	195.59	0.200 ± 0.011
53088.299	293.18	191.18	0.203 ± 0.013
53088.314	290.95	187.43	0.209 ± 0.012
53088.329	289.54	183.33	0.205 ± 0.013
53088.340	289.19	180.37	0.208 ± 0.013
53088.351	289.39	177.45	0.198 ± 0.017
53092.231	307.94	204.26	0.183 ± 0.021
53092.250	302.49	200.41	0.191 ± 0.016
53093.148	328.43	216.70	0.115 ± 0.012
53093.163	325.90	214.97	0.112 ± 0.013

Table 1—Continued

MJD	Projected Baseline (m)	Baseline Position Angle (deg)	Calibrated Visibility
53093.179	322.24	212.79	0.110 ± 0.007
53093.199	316.93	209.74	0.131 ± 0.010
53093.223	309.63	205.36	0.146 ± 0.014
53093.239	304.84	202.15	0.160 ± 0.011
53093.256	300.01	198.40	0.151 ± 0.018
53093.335	289.30	178.12	0.137 ± 0.012
53095.249	243.70	130.75	0.433 ± 0.041
53103.200	312.56	254.45	0.263 ± 0.026
53103.219	307.95	252.80	0.234 ± 0.020
53103.239	298.97	250.74	0.310 ± 0.021
53103.259	285.76	248.24	0.318 ± 0.044
53104.216	307.92	252.79	0.262 ± 0.031
53104.236	299.02	250.75	0.281 ± 0.033
53105.261	278.11	130.25	0.340 ± 0.044
53105.279	278.34	128.86	0.320 ± 0.031
53106.282	277.96	128.48	0.276 ± 0.028
53107.290	276.77	127.91	0.259 ± 0.026
53108.255	278.23	130.09	0.284 ± 0.038
53108.274	278.14	128.63	0.310 ± 0.045
53111.265	260.88	187.19	0.227 ± 0.022
53111.281	259.59	182.72	0.189 ± 0.018
53111.291	259.37	180.40	0.255 ± 0.017
53111.300	259.61	177.17	0.213 ± 0.021
53111.314	260.72	173.20	0.212 ± 0.016
53111.324	262.02	170.49	0.207 ± 0.017

Table 2. Interferometric Measurements of the Check Star (HD 88547)

MJD	Projected Baseline (m)	Baseline Orientation (deg)	Calibrated Visibility
53074.369	205.43	145.59	0.560 ± 0.068
53074.384	207.80	144.20	0.519 ± 0.074
53078.246	214.24	136.51	0.563 ± 0.033
53078.267	225.06	133.10	0.551 ± 0.039
53078.286	233.75	130.61	0.532 ± 0.060
53079.222	201.50	141.20	0.666 ± 0.097
53079.250	217.65	135.41	0.519 ± 0.068
53080.267	217.75	200.73	0.522 ± 0.050
53080.331	206.12	185.08	0.585 ± 0.049
53081.181	240.14	214.04	0.512 ± 0.048
53081.208	233.51	210.73	0.455 ± 0.045
53081.243	223.58	204.98	0.591 ± 0.070
53081.287	212.36	195.60	0.548 ± 0.081
53081.322	206.53	186.73	0.574 ± 0.064
53081.354	205.36	178.02	0.528 ± 0.033
53088.230	298.34	208.59	0.300 ± 0.020
53088.267	282.95	200.93	0.309 ± 0.025
53088.287	275.86	195.99	0.364 ± 0.019
53093.153	322.30	217.29	0.279 ± 0.028
53093.168	317.64	215.72	0.318 ± 0.027
53093.187	310.57	213.29	0.319 ± 0.026
53093.211	300.64	209.54	0.324 ± 0.022
53093.228	293.42	206.43	0.401 ± 0.024
53093.246	286.07	202.73	0.439 ± 0.034
53093.261	280.27	199.24	0.404 ± 0.039
53095.254	239.28	129.06	0.474 ± 0.060
53103.207	310.56	254.96	0.292 ± 0.031
53103.224	304.43	254.14	0.332 ± 0.036
53103.245	292.83	252.89	0.374 ± 0.025
53103.264	278.05	251.37	0.409 ± 0.050
53104.222	304.38	254.14	0.351 ± 0.028
53104.241	293.38	252.94	0.369 ± 0.031
53105.267	276.40	129.57	0.413 ± 0.051
53105.285	278.32	128.73	0.440 ± 0.043
53106.287	278.48	128.55	0.424 ± 0.050
53107.296	278.19	128.27	0.427 ± 0.050
53108.262	277.03	129.35	0.421 ± 0.042
53108.283	278.49	128.52	0.421 ± 0.056
53111.271	238.95	186.96	0.522 ± 0.042
53111.330	241.57	168.73	0.518 ± 0.041

Table 3. Parameters of Stellar Models for Regulus

		From Spectroscopy							From Interferometry				
i (deg)	β	$V \sin i$ (km s^{-1})	V_e/V_c	R_p ($R_\odot$)	R_e ($R_\odot$)	M ($M_\odot$)	T_p (K)	T_e (K)	$R_{\rm minor}$ (mas)	$R_{\rm major}$ (mas)	α (deg)	$d/d(Hipparcos)$	χ^2_ν
90	0.00	305	0.82	3.15	4.05	3.45	12280	12280	0.624	0.802	87.4	0.988	3.95
90	0.05	307	0.82	3.15	4.06	3.45	12825	11968	0.624	0.806	87.2	0.987	3.76
90	0.10	309	0.83	3.14	4.07	3.45	13400	11643	0.626	0.810	86.8	0.984	3.58
90	0.15	310	0.83	3.14	4.08	3.46	14006	11309	0.625	0.811	86.1	0.984	3.45
90	0.20	314	0.84	3.14	4.12	3.43	14660	10852	0.624	0.816	86.0	0.987	3.38
90	0.25	317	0.86	3.14	4.16	3.39	15400	10314	0.623	0.825	85.5	0.988	3.35
90	0.30	323	0.87	3.15	4.22	3.39	16235	9677	0.619	0.830	85.3	0.994	3.39
90	0.35	326	0.88	3.14	4.24	3.39	17120	9155	0.620	0.836	84.6	0.993	3.55
80	0.00	305	0.83	3.13	4.05	3.45	12280	12280	0.626	0.804	87.6	0.987	3.97
80	0.05	307	0.83	3.12	4.06	3.45	12836	11943	0.627	0.807	87.2	0.985	3.78
80	0.10	309	0.84	3.12	4.07	3.45	13420	11589	0.626	0.809	86.8	0.985	3.61
80	0.15	310	0.84	3.12	4.08	3.45	14035	11220	0.628	0.814	86.6	0.982	3.48
80	0.20	314	0.85	3.12	4.12	3.44	14686	10740	0.626	0.818	86.1	0.985	3.40
80	0.25	317	0.87	3.12	4.16	3.41	15435	10191	0.625	0.825	85.9	0.987	3.36
80	0.30	323	0.88	3.12	4.22	3.40	16280	9486	0.625	0.835	85.7	0.988	3.36
75	0.00	305	0.84	3.10	4.05	3.46	12280	12280	0.626	0.803	87.7	0.988	3.98
75	0.05	307	0.85	3.10	4.07	3.46	12845	11905	0.629	0.808	87.3	0.985	3.80
75	0.10	309	0.85	3.10	4.08	3.46	13442	11516	0.629	0.810	86.9	0.985	3.64
75	0.15	310	0.85	3.10	4.09	3.46	14068	11109	0.630	0.814	86.7	0.983	3.51
75	0.20	314	0.86	3.10	4.12	3.44	14740	10581	0.630	0.821	86.5	0.983	3.43
75	0.25	317	0.88	3.10	4.17	3.40	15510	9953	0.630	0.830	86.5	0.983	3.38
70	0.00	305	0.86	3.06	4.06	3.46	12280	12280	0.628	0.804	87.6	0.987	4.02
70	0.05	307	0.86	3.06	4.07	3.47	12862	11849	0.629	0.808	87.5	0.985	3.85
70	0.10	309	0.87	3.06	4.08	3.46	13476	11401	0.630	0.813	87.3	0.982	3.70
70	0.15	310	0.87	3.06	4.09	3.47	14119	10942	0.634	0.816	86.9	0.980	3.57
70	0.20	314	0.88	3.06	4.13	3.45	14800	10336	0.635	0.825	87.1	0.979	3.50
70	0.25	317	0.90	3.06	4.17	3.41	15585	9618	0.634	0.833	87.2	0.980	3.46

Table 4. Parameter Estimates from Different Models

Parameter	Uniform Ellipsoid	Grid Search	Spectroscopically Constrained
No. parameters	3	6	4
$R_{\rm minor}$ (mas) ..	0.651 ± 0.016	0.627 ± 0.015	0.623 ± 0.006
$R_{\rm major}$ (mas) ..	0.771 ± 0.032	0.810 ± 0.023	0.825 ± 0.008
α (deg)	84.9 ± 2.4	83.7 ± 2.5	85.5 ± 2.8
i (deg)	···	85^{+5}_{-9}	90^{+0}_{-15}
β	···	0.13 ± 0.05	0.25 ± 0.11
χ^2_ν	3.41	3.73	3.35

Table 5. Final Parameters for Regulus

Parameter	Value
$\Theta_{\rm minor}$ (mas) ...	1.25 ± 0.02
$\Theta_{\rm major}$ (mas) ...	1.65 ± 0.02
α (deg)	85.5 ± 2.8
i (deg)	90^{+0}_{-15}
β	0.25 ± 0.11
$V \sin i$ (km s^{-1})	317 ± 3
V_e/V_c	0.86 ± 0.03
R_p ($R_\odot$)	3.14 ± 0.06
R_e ($R_\odot$)	4.16 ± 0.08
M ($M_\odot$)	3.4 ± 0.2
T_p (K)	15400 ± 1400
T_e (K)	10314 ± 1000
$< T >$ (K)	12901 ± 500
L ($L_\odot$)	347 ± 36
d (pc)	23.5 ± 0.4
A_V (mag)	0.016 ± 0.010